Local topography effects on the surface temperatures on Mars -Application to the case of Recurring Slope Lineae (RSL)

Cédric Millot, Cathy Quantin-Nataf, Cédric Leyrat, Maxime Enjolras

Local topography effects on the surface temperatures on Mars – Application to the case of Recurring Slope Lineae (RSL)

Cédric Millot[1], Cathy Quantin-Nataf[1], Cédric Leyrat[2], and Maxime Enjolras[1]

[1]Univ Lyon, Univ Lyon 1, ENSL, CNRS, LGL-TPE, F-69622, Villeurbanne, France
[2]Observatoire de Paris, CNRS UMR8109, Université PSL, Sorbonne Université, Université Paris-Diderot

February 17, 2025

Abstract

Recurring Slope Lineae (RSL) are dark linear recurrent features which incrementally lengthen and fade each year on Martian slopes. Their activity during warmest seasons rises the question of modern martian water related process. To investigate this question, this study focuses on the thermal context of slopes hosting RSL. The paper presents a numerical study of surface and subsurface temperatures at high spatial resolution (1 m/pix) of three well-described RSL sites: Palikir Crater, Coprates Chasma and Rauna Crater. We then compare our local thermal simulations to quantitative measurements of the length and timing of RSL lengthening and fading in these three sites. We underline that RSL sites surface temperatures are poorly correlated with RSL morphology's changes. Indeed, lineae lengthening occurs while surface temperature are under the melting point of pure water (273 K) for at least two sites: Coprates Chasma and Rauna Crater, for two different sets of surface physical properties. We also highlight the significant differences in temperature range while lengthening occurs for all the sites, from ∼220 K in Coprates Chasma site to a maximum of ∼300 K in Palikir Crater. RSL are sometimes associated with signals in topography, involving significant heating variations of the surface, which can yield to the formation of local winds. Facing the thermal inconsistency between wet triggering processes and RSL reported activity, we suggest that RSL are more probably dry processes.

Keywords: RSL, temperatures, morphology, topography, modern Mars

1 Introduction

Modern Mars climate is cold and dry excluding liquid water to be stable on largest part of the surface (e.g. Baker et al., 1991; Pollack et al., 1987), excepted for equatorial locations and large impact basins (Haberle et al., 2001). The recent discoveries of dark linear structures recurrent over the years during warm seasons has yielded to a reconsideration of our knowledge. These features, called Recurring Slope Lineae (RSL, McEwen et al., 2011) are commonly characterized from orbital survey data by a localized decrease of albedo of linear structures that follow local slopes. RSL are small scale geological processes: a few hundred meters in length and width for a typical area and no more than a few meters width for a single linea. They have been defined according to three criteria: first, they present an incremental lengthening; second, they fade and possibly completely disappear; finally, they recur over multiple Mars years. Their activity has been interpreted alternatively as liquid water or brine flows due to ice melting or subsurface aquifers (e.g. McEwen et al., 2011, 2014; Stillman et al., 2014). The possibility of current seasonal water seepages at the surface of Mars may have a large impact on modern potential habitability knowledge and implications for Mars human exploration. Hydrated salts have been tentatively detected at a few well-known RSL sites (Ojha et al., 2015), which was considered as the first indirect evidence for the presence of liquid water on Mars present days,

even if these detections have been recently questioned (Vincendon et al., 2019) as most of them seem to be products of CRISM (Compact Reconnaissance Imaging Spectrometer for Mars, Murchie et al., 2007) artefacts. Hence, during the first part of the last decade, RSL have been mostly considered as wet flows, alternately as freshwater flows (McEwen et al., 2011, 2014) or brines (Chevrier and Rivera-Valentin, 2012), sometimes with a subsurface aquifer origin (Stillman et al., 2016). Adsorption of atmospheric moisture on salts at the surface yields to deliquescence process, also able to produce flows. Experimental studies of deliquescence have been performed (Gough et al., 2011, 2014, 2016) to determine the Deliquescence Relative Humidity (DRH) necessary to trigger the deliquescence process for various perchlorates, supported by the possible detections of hydrated salts, especially perchlorates, on known RSL sites (Ojha et al., 2015). Magnesium and sodium-perchlorates mixtures can persist at relatively low Relative Humidity (RH), with 17% for Mg mixture, 15% for Na mixture (Gough et al., 2014). Calcium chlorides are also persistent over half a sol and metastable until very low RH (∼4.0%, Gough et al., 2016). However, more recent studies have challenged wet hypotheses. First, thermophysical analyses using THEMIS (THermal EMission Imaging System, Christensen et al., 2004) data suggest that RSL contain limited amount of water (0.5 - 3%wt, Edwards and Piqueux, 2016). Another challenge for water-related processes is the recent questioning (Vincendon et al., 2019) about reliability of all the hydrated salts detections from Ojha et al., 2015 which are interpreted as CRISM well-known artefacts. Moreover, liquid water is not stable at the surface on most southern hemisphere locations on Mars due to the low atmospheric pressure (e.g. Hess et al., 1979) which does not exceed the water triple point (see Haberle et al., 2001, their figure 8).

The difficulty to reconcile liquid water and RSL characteristics have risen dry mechanisms. Some studies involve grainflows (Dundas, 2020; Dundas et al., 2017b) or dust erosion (Vincendon et al., 2019) induced by local winds or gas-triggering mechanisms (Schmidt et al., 2017) using enhanced Knudsen pump (De Beule et al., 2014). These dry processes are linked to the thermal behavior of the local medium, as Knudsen pump depends on vertical temperature gradient (Schmidt et al., 2017) and slope winds can be induced by local differences in temperatures (thermal winds, e.g. Gierasch and Sagan, 1971). Hence, dry or wet, most of the RSL proposed mechanisms are linked to the thermal properties of the ground. Thus, an accurate assessment of the temperature field on RSL sites is required to discriminate these hypotheses. In this study, we develop a combined approach to study several RSL sites. In a first part, we use orbital imagery at high resolution from High Resolution Imaging Science Experiment (HiRISE, McEwen et al., 2007) to describe and perform measurements of RSL length variations over the years, at three confirmed RSL sites. In a second part, we estimate the solar incoming energy during a martian year for three well-known RSL sites, in order to compute surface and subsurface temperatures (up to few meters depth) by solving the heat equation using a Mars thermal model (Clifford and Bartels, 1986) at sub-meter spatial scale. Temperature computations are made for two sets of physical parameters: one set models a constant dry (or nearly dry) surface, the other describes alternately dry and wet surfaces correlated with RSL activity during a year. We investigate the three RSL sites at different locations on Mars to retrieve their seasonal cycle variations and compare them with seasonal temperature variations at the surface and the subsurface. Horizontal insolation and temperature variations induced by local topography are assessed to challenge previously proposed RSL triggering mechanisms. Finally, we aim to provide a complementary assessment of the previous results by measuring RSL over the seasons and computing surface and subsurface temperatures for an area presenting numerous RSL.

2 Data and Methods

It is known that RSL activity varies with locations (e.g. Stillman et al., 2017). In the goal to quantify the RSL growth and compare it with insolation, surface and subsurface (few meters depth) temperatures, we choose several RSL sites on Mars. The chosen RSL sites in this study must respect some technical criteria. First, sites must display confirmed RSL, which means that lineae recur over multiple Mars years and have an incremental growth (Ojha et al., 2014). We also need sufficient temporal coverage of the studied RSL sites by continuous orbital survey of the slope lineae on at least one Martian Year (MY, Clancy et al., 2000). We focus on three different sites (figure 1) which satisfy

all our criteria in Rauna Crater, located in Rauna Crater (RC, figure 1A), Coprates Chasma (CC, figure 1B and C) and Palikir Crater (PC, figure 1D). The three sites containing RSL are located in three distinct regional contexts on Mars: equatorial latitudes, southern mid-latitudes and north hemisphere, mostly in RC (Stillman, 2018). In CC site, RSL are observed on all slope orientations (Chojnacki et al., 2016). So we track variations on RSL activities and surface and subsurface temperatures making lineae length measurements for two main orientations (northwest and southwest) at similar latitude and longitude values within CC (see section 3.1); this approach aims to estimate the seasonal differences of thermal properties between two representative slope orientations of RSL areas. Indeed, different orientations imply variations in surface heating by the sun and by extension different surface and subsurface temperatures (McEwen et al., 2014).

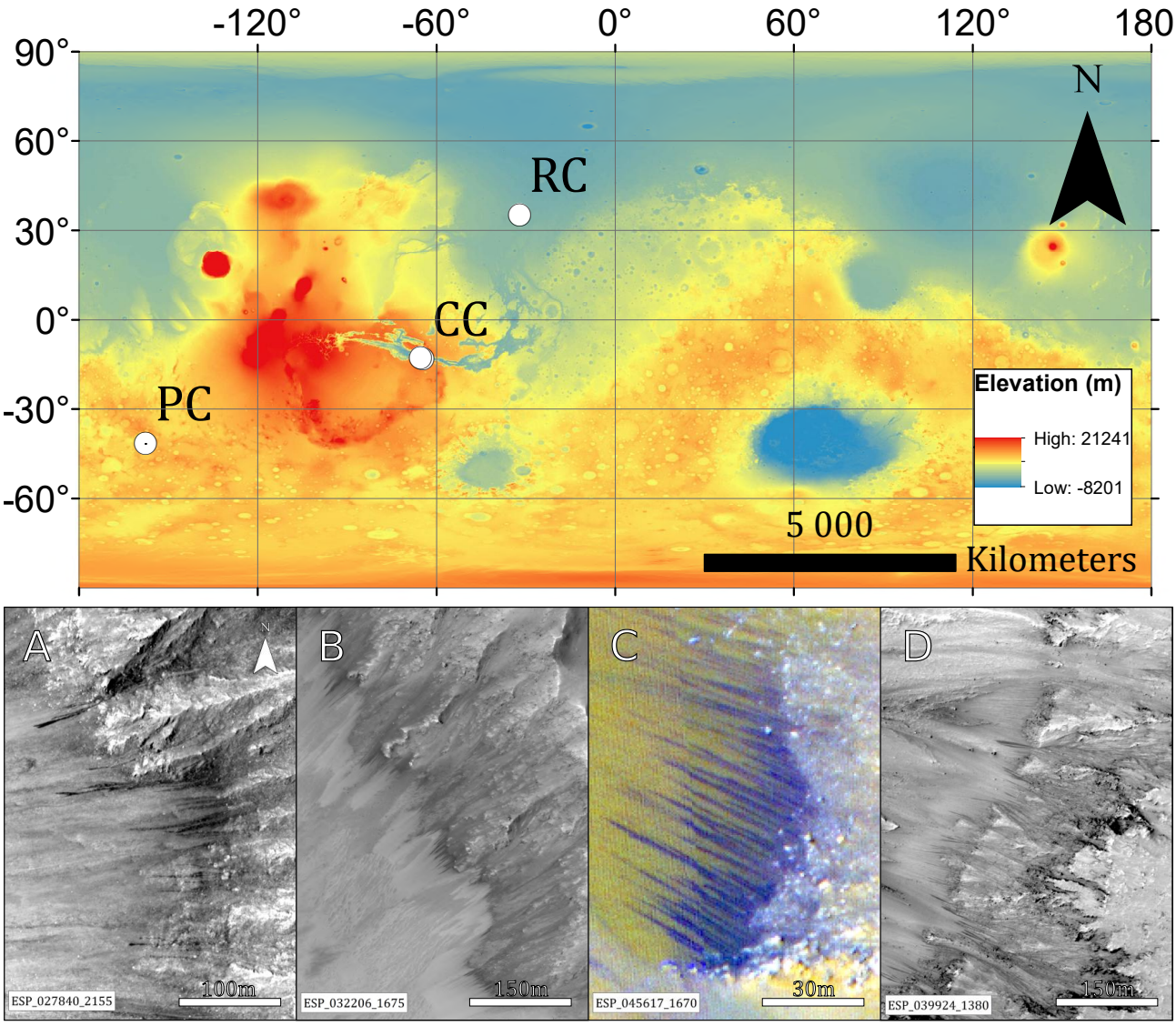

Figure 1: Top: RSL sites for this study on the global MOLA map. Colorscale indicates the elevation. Bottom: RSL in A) Rauna Crater (RC) B) Coprates Chasma, southwest orientation (SW-facing CC) C) Coprates Chasma, northwest orientation (NW-facing CC, HiRISE MIRB color) and D) Palikir Crater (PC).

Thermal models (that include MarsTHERM Clifford and Bartels, 1986; insolation program from Leyrat et al., 2016) have been used in our study to compute insolation, surface and subsurface temperatures on Mars at high resolution. Thermal models are widely involved in RSL studies, most of the time to determine the melting temperature of RSL and compare it with water or brines (e.g. Chevrier and Rivera-Valentin, 2012), to challenge the RSL wet hypotheses (Edwards and Piqueux, 2016) or model

RSL with multiple wet and dry layers (Stillman et al., 2017, with MRAMS model from Michaels and Rafkin, 2008). THEMIS (Christensen et al., 2004) and TES (Thermal Emission Spectrometer, Christensen et al., 2001) data are used to determine the brightness temperatures at the surface (McEwen et al., 2014; Ojha et al., 2014), but these data are restricted to lower spatial resolution than RSL requirements. We modified MarsTHERM thermal model to include orbital data as Digital Elevation Models (DEM) at RSL submetric scales to take into account the small scale topographic effects. While recent study uses high resolution thermal model to focus on shadowing, small scale topography and CO_2 frost patches at Palikir Crater site (Schorghofer et al., 2019), we concentrate our analysis on insolation and surface temperature variability induced by small scale topography on three different sites, including Palikir Crater, to provide a complementary work. Our study combines two different approaches: a RSL description from observations using orbital data and the simulation of insolation, surface and subsurface temperatures using thermal models.

2.1 Orbital data combination

We use HiRISE (High Resolution Imaging Science Experiment) images with a spatial resolution of 25-50 cm per pixel to image the RSL (McEwen et al., 2007). HiRISE data are also used to produce DEM from stereophotogrammetry with a spatial resolution around 1 m/pixel, for a vertical precision of few tenths of centimeters (Kirk et al., 2008; Sutton et al., 2015). Some HiRISE DEM have been released by HiRISE team. From these DEM, we estimate local topography (slopes, orientations) using Geographic Information System (GIS) software tools on HiRISE camera products (McEwen et al., 2007). When possible, we use the orthorectified (projected onto the surface from MOLA altimeter data, Kirk et al., 2008) products from the HiRISE team to avoid any topographic distortion (Kirk et al., 2008). Interpolated or faceted areas and other known artefacts (CCD seams and boxes, see the HiRISE team website for further explanation and Kirk et al., 2008) have been carefully removed to provide the most accurate measurements on RSL. Faceted areas are the main artifact that is present on RSL areas, often located on visually homogenous terrains from HiRISE data. They are caused by the lack of matching features between the two HiRISE images used to make the DEM (Kirk et al., 2008). In addition, to investigate the context of the RSL studied here, we use images with a lower resolution but a larger surface coverage, such as HRSC (High Resolution Stereo Camera) images from Mars Express (Neukum and Jaumann, 2004) and their associated DEM products (∼75 m/px) or MOLA (Mars Observer Laser Altimeter) DEM (Zuber et al., 1992, ∼500 m/px), depending on the surface of the area we consider.

2.2 RSL lengths measurements

We make RSL length measurements to provide us a quantitative assessment of their activity over time and underline the different periods when RSL are growing, stable or fading. First, we identify single lineae and its evolution through time; then lineae lengths are measured under GIS environment at different time of the martian year (figures 2 and 4B). We define lineae origins as invariant points from which we define the length of the RSL. Hence, an initial set of lineae is defined and we keep the same lineae over all the images (figure 2). Our length measurements (L_m) are then corrected by the local slopes determined from HiRISE DEM for the small RSL areas as

$$L = \frac{L_m}{\cos \alpha}, \tag{1}$$

where L_m is the apparent length derived from our measurements, α is the local slope in degrees and L is the real RSL length. Neighbor dark lineae have not necessarily similar activities; some lineae grow between two HiRISE images whereas others do not change or even fade. We determine how important the spatial length variability is between the lineae from a same set, i.e. a same image. We create an index $F_i = \sigma_i / \overline{L_i}$ to describe this spatial variability, where i is the number of images over a site, σ_i is the standard deviation of length measurements for one image and $\overline{L_i}$ is the mean. Notice that F does not describe the seasonal length variations, it estimates the length dispersion on one image. Errors on F are computed assuming an error on length measurement of 2 meters (1 meter for each

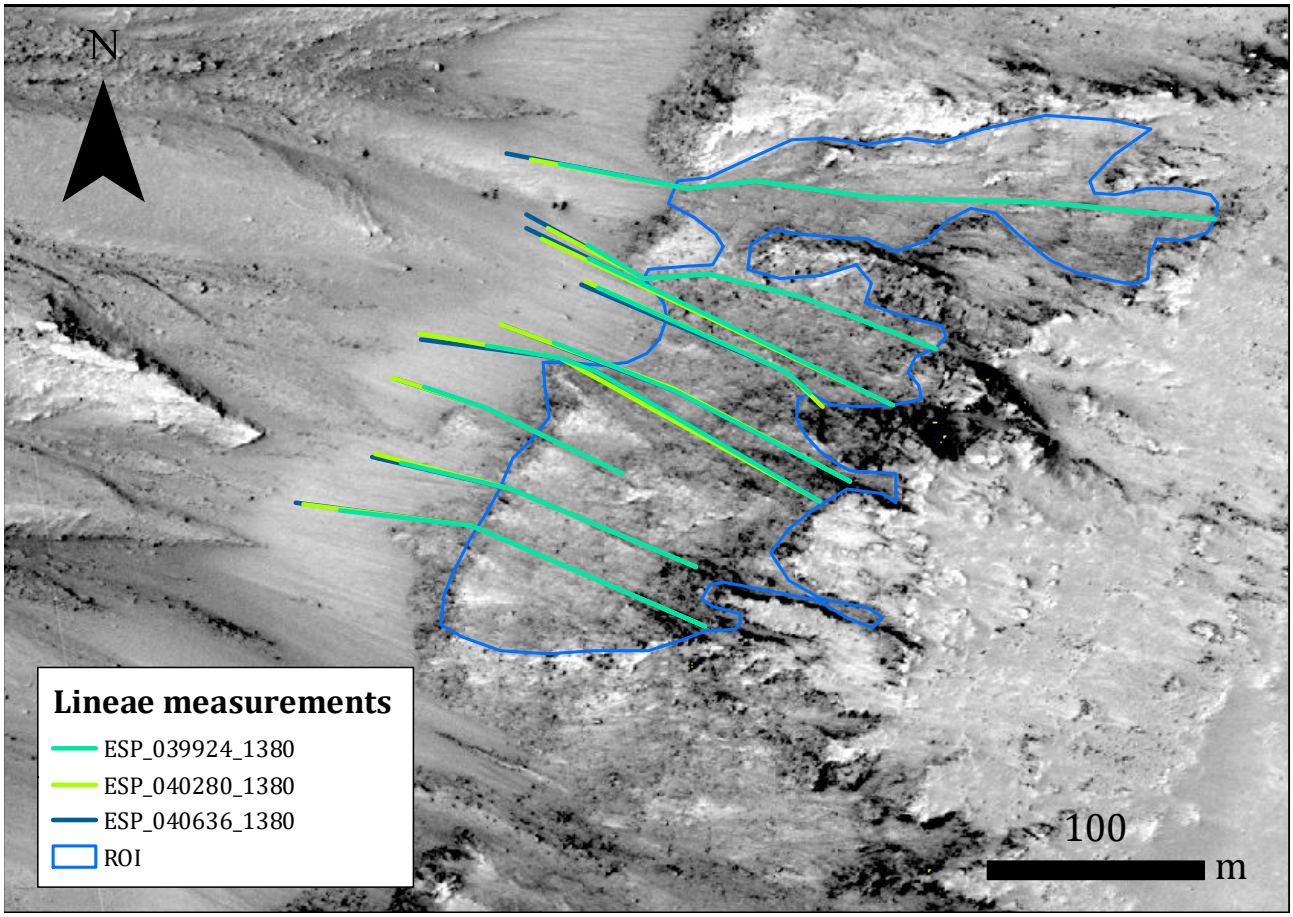

Figure 2: Example of lineae length measurements for successive HiRISE images ESP_039924_1380, ESP_040280_1380 and ESP_040636_1380 in PC site. Lineae start from an invariant point at the top of the Region of Interest (ROI). Background image is ESP_040636_1380.

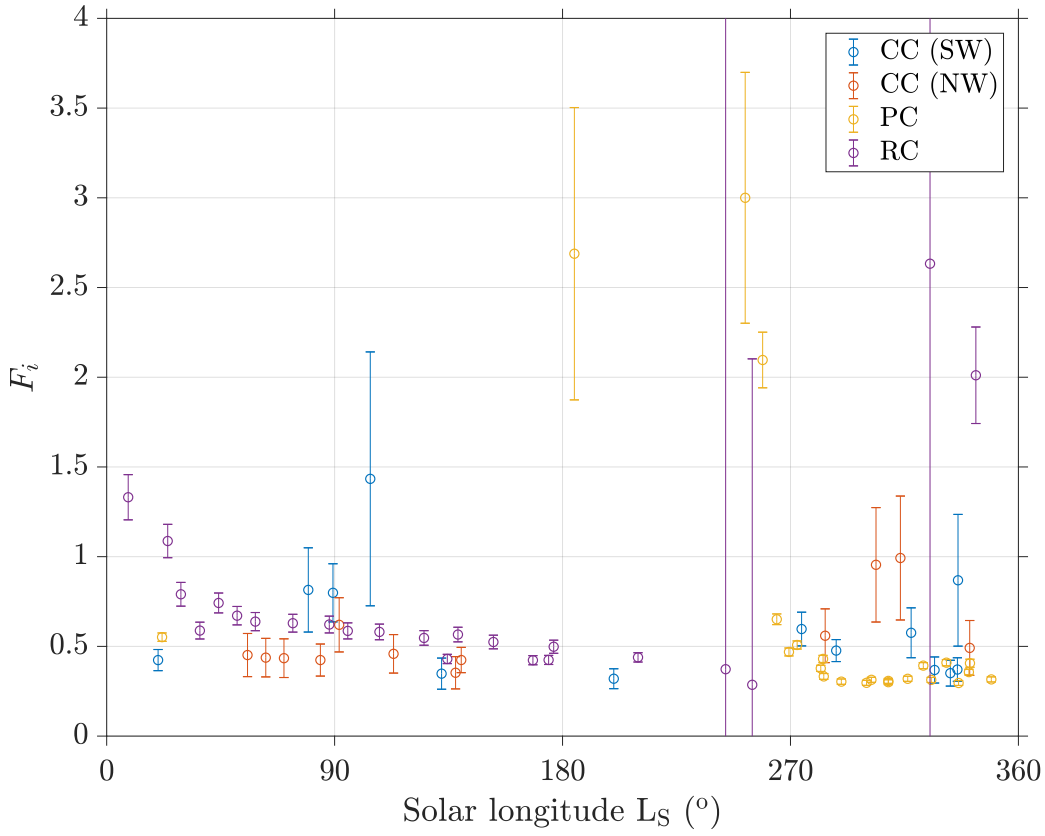

Figure 3: Dispersion index F_i as a function of site and solar longitude. A low F_i means a low dispersion on data regarding the mean value.

line endpoint, as HiRISE camera solves submetric object), which are propagated on F using the sum of relative uncertainties $d\sigma_i/\sigma_i$ and $d\overline{L_i}/\overline{L_i}$ as:

$$dF_i = \frac{d\sigma_i}{\sigma_i} + \frac{d\overline{L_i}}{\overline{L_i}}. \tag{2}$$

Figure 3 highlights the length variability in our measurements, normalized by the mean length for each image, for different solar longitudes. Colors indicate the site we consider. Low values of F_i underlines the low dispersion value against the mean value, whereas F_i is high when dispersion against mean is high, which can traduce length variations for a limited number of lineae. It is the case for PC site (yellow dots in figure 3) between L_S ~180 and $L_S \sim 250°$, where a single linea is lengthening. Overall, dispersion is limited as only 8 on 76 values ($\sim 10\%$) are above $F_i = 1$ (4 for RC site, 3 for PC site and 1 for CC (SW) site). Thus, such activity is marginal in our observations and a general trend (e.g. lengthening phase) can be observed for all our set of lineae. Hence, we aim to use a single length value for each HiRISE image to provide a better comprehension of seasonal length profile. We take the mean length value $\overline{L_i}$ for each image to make the seasonal length profile presented in the results (figure 9). Notice that we also make morphological descriptions of the RSL using HiRISE imagery, associated to measurements when length variations are not sufficient enough to fully describe the RSL activity, for instance when RSL has albedo changes but keep the same length (see figure 9). The detail of the morphological description of the RSL is available in the supplementary data of this paper.

2.3 Topography

From the DEM, we can compute several parameters that describe the local topography of RSL such as slopes, orientations and elevations. These three parameters are determined for each pixel of

the considered DEM located on a RSL zone using GIS tools. In this study, we mainly use HiRISE DEM (Kirk et al., 2008) which provides the best resolution for a DEM on Mars (1 m/pixel), allowing to catch thin details by few meters width such as RSL features.

Local elevations Local elevations are provided by HiRISE DEM (see Kirk et al., 2008 and HiRISE team website). To reduce computation time for further steps described in this section, we clip the data around RSL areas to define Regions of Interest (ROI) (figure 4B). These selections allow to keep reasonable arrays' sizes on which the local diurnal and seasonal insolations will be computed to derive the surfaces and subsurface temperatures. We also pay attention to the absence of artifacts within the ROI such as "Maltese cross" polygonal artifacts or smoothed/interpolated areas (Kirk et al., 2008) which may not contain enough topographic information. These types of artifacts or smoothed terrains could be numerous around RSL areas on HiRISE DEM, especially in what we visually observe and interpret as fine-grained and homogeneous material, where RSL are often the most visible on optical imagery. The ROI for insolation and temperature computations is restricted to the areas where metric objects can be resolved using HiRISE images (McEwen et al., 2007). We visually exclude areas where manual interpolations are apparent on the associated DEM (Kirk et al., 2008). ROI in figure 4B does not fully cover lineae, as termination points are located within an interpolated area. Thus, we exclude lowest part of RSL from the ROI to keep non-interpolated parts of the DEM. Once this verification has been done, we use the DEM to provide slope and aspect (direction of the slopes) values for every pixel.

Local slopes ArcGIS software has been used to estimate the slope using the Spatial Analyst Toolbox. Slope values have been computed using the planar method (Burrough et al., 2015). This tool provides a slope value θ between 0 and 90° for each pixel according to the elevation

$$\theta = \arctan(\sqrt{(\frac{dz}{dx})^2 + (\frac{dz}{dy})^2}), \tag{3}$$

where dz/dx and dz/dy are the longitudinal and latitudinal elevation gradients, calculated from weighted pixel elevations in x and y direction. For further explanation, the reader is referred to the description of the tool on ArcGIS website.

Local orientations The local orientation of DEM elements with respect to the North/South axis direction, so called "aspect value", is required to compute to local solar absorbed flux. For instance, an element of the surface with a west-facing slope will be heated after an east-facing slope during the day. In our work, we sort the aspect values according to eight azimuth classes (every 45°), as presented in the figure 4. To compute azimuth angle at every point of our DEM, we use the "Aspect" tool from the ArcGIS software. Once DEM elevations, slopes and orientations have been locally estimated, one can use those values to compute the local insolation versus time, across a full seasonal cycle, accounting for diurnal variations (Leyrat et al., 2016).

2.4 Thermal modeling at surface and subsurface

Temperatures of surfaces and subsurfaces are mainly driven by the incoming solar flux received at the surface of Mars. Thus, their estimations require an accurate and local estimation of this flux over time, similarly to Leyrat et al., 2016.

We aim to constrain temperature field at RSL spatial scales and assess temperature seasonal variations. For each pixel, insolation is computed every 30 minutes in order to resolve the diurnal insolation cycle ($\sim$ 24h40). HiRISE images are acquired between 1.00 and 3.30 p.m: we do not have information of RSL activity from orbital imagery at different local times for our sites, even if a recent study (Munaretto et al., 2020) has been released on Hale Crater site using CaSSIS (Thomas et al., 2017) data at different local hours. We resolve diurnal cycle in order to better constrain the thermal state in which RSL occur. Moreover, we perform computations using MarsTHERM model (Clifford and Bartels, 1986) over a complete martian year with an error in time equal to half a time step duration,

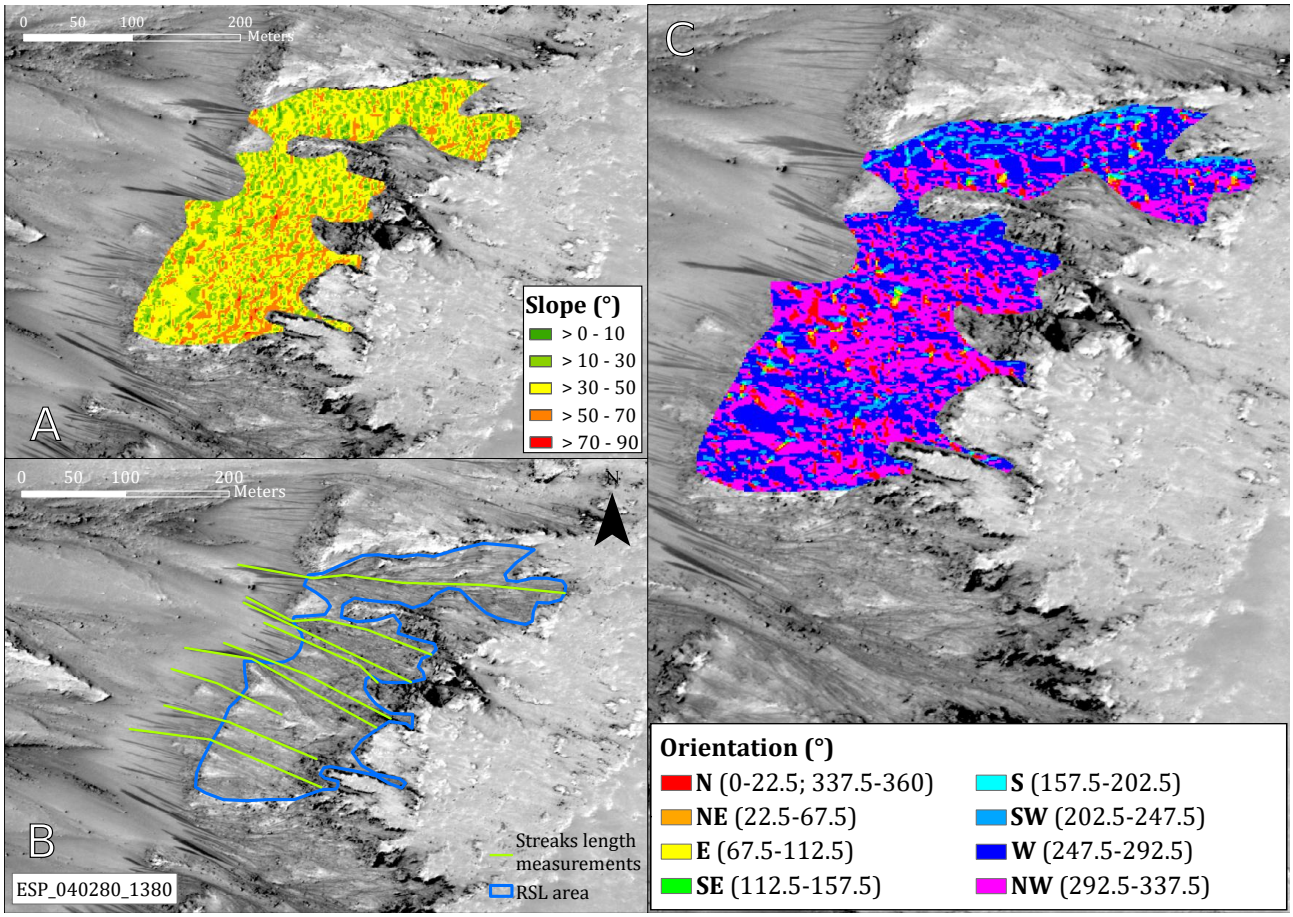

Figure 4: A) Local slope values, computed with the local DEM. B) RSL area on which we perform our temperature computations and the associated measurements for HiRISE image ESP_040280_1380. C) Local azimuths extracted for the same local DEM than slopes.

that is to say 15 min. For each pixel, the output of the model contains, surface and subsurface temperature variations with time, that directly depends on surface heating, local topography and physical parameters such as thermal inertia.

2.4.1 Local Insolation

The orbital parameters, as the obliquity, the eccentricity or the argument of perihelion, have a direct influence on the insolation and by extension, the seasons. Insolation can be calculated using the following equation:

$$q_{\odot} = \frac{E_{\odot}}{d^2} \cos i \tag{4}$$

where $q_{\odot}$ is the insolation in W m^{-2}, $E_{\odot}$ is the solar constant (= 1368 W m^{-2}), d is the heliocentric distance in astronomical units (AU) and i is the incidence angle. The SPICE (Spacecraft Planet Instrument C-matrix Events)/NAIF (Navigation and Ancillary Information Facility) libraries (Acton, 1996) are used to account for the Martian's orbital parameters. At RSL locations, the local solar time (LST) is estimated from the UTC time of orbital HiRISE data. The time step Δt for our computations is fixed to 1/50 of a sol duration to grab diurnal variations, but a longer time step may be more efficient in terms of CPU computation time for large areas with HiRISE imagery. Mars has an orbital revolution period approaching 669 sols (= martian day), so calculations for a single pixel yield to 50×669 = 33450 time steps per year.

Model outputs are temporal maps of insolation. An example is represented on figure 5. Figure 5A illustrates how east-facing slopes receive sunlight before west-facing slopes, whereas they are in the shadows at the end of the day in PC site, from 200 W.m^{-2} on east-facing walls to 600 W.m^{-2} on west-facing slopes around 3 p.m. This insolation map mimics qualitatively THEMIS derived temperatures from Ojha et al., 2014 which shows significant temperature differences between western and eastern crater walls. Locally, the duration of illumination varies depending on the orientation (figure 5B). Variability in day duration is higher for south-facing slopes than for north-facing ones. Eastern and western-facing slopes receive a similar duration, with slightly higher variations than north-facing slopes. In the end, insolation variations are due to variable incident sunlight induced by different incidence angles (figure 5C). Southern seasonality is characteristic for all orientations, with a maximum peak slightly before solar longitude $L_S = 270°$, due to combined effects of summer solstice (at $L_S = 270°$) and perihelion (at $L_S = 251°$).

2.4.2 Thermal Model

To evaluate the surface and subsurface temperatures of the selected RSL area, we use a thermal model called MarsTHERM described in details by Clifford and Bartels, 1986. MarsTHERM computes local temperatures at surface and subsurface taking into account the position and inclination of Mars on its orbit, the local slope, the orientation and the albedo of the surface, the geographic coordinates and the physical properties of the ground such as thermal inertia. It uses finite differences scheme in order to solve the energy balance at the surface and the vertical heat transfer by conduction (Clifford and Bartels, 1986). Calculations are performed on layers whose thicknesses increase with depth to optimize computation time. Time step is adaptive in depth direction, also growing with deeper layers. Lateral heat transfer is neglected at the DEM scale, this latter being much larger than the typical thermal skin depth.

Physical parameters The heat transfer efficiency through planetary surfaces depends strongly on the thermal inertia I that drives the conduction process. Deriving thermal inertia I is not trivial as it depends on the thermal conductivity k and the density ρ (e.g. Cunningham et al., 2017; Piqueux and Christensen, 2011):

$$I \equiv \sqrt{k\rho c} \tag{5}$$

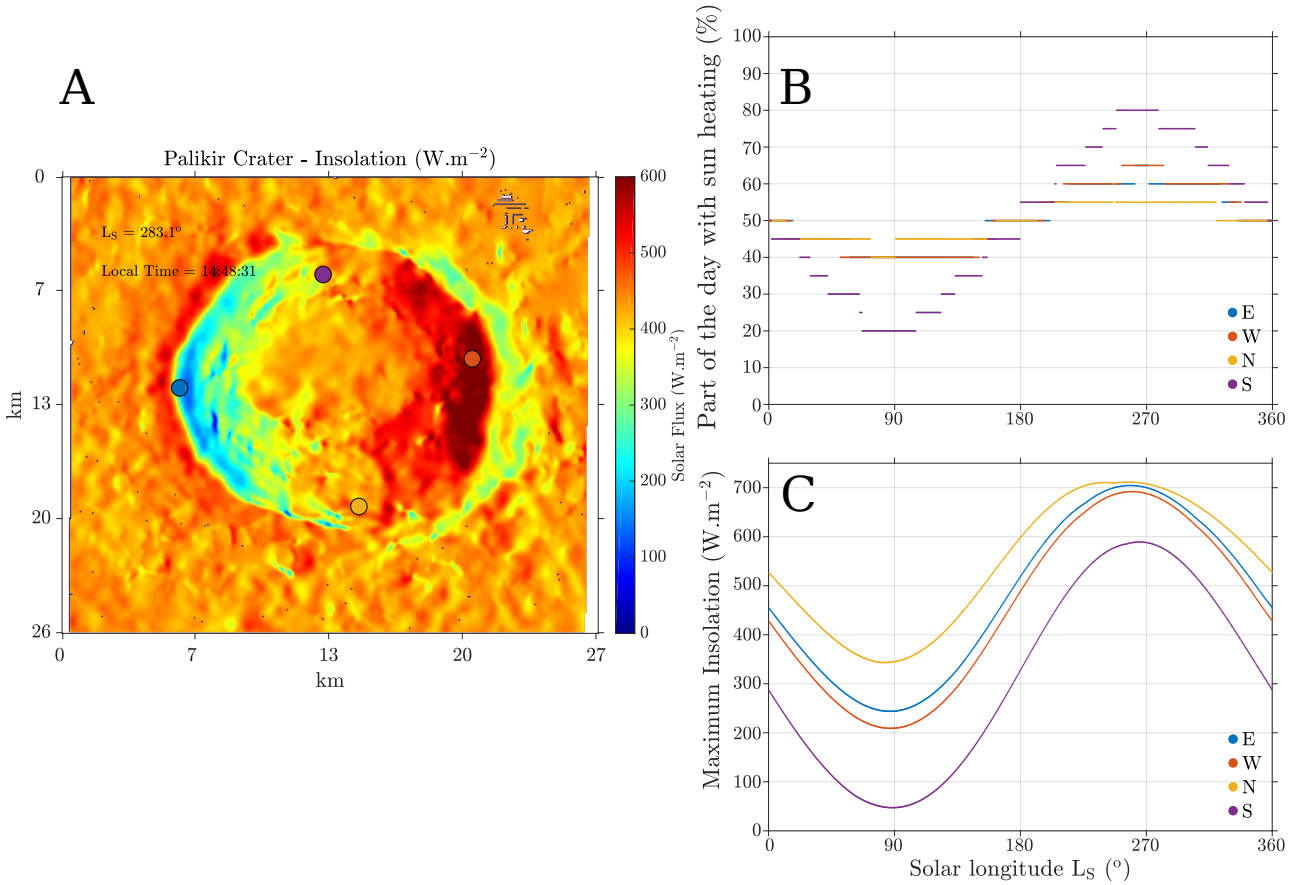

Figure 5: A) Computed solar fluxes in W.m^{-2} at Palikir Crater in southern mid-latitudes site (41.6°S, 202.3°E). B) Part of the day with sun heating for four pixels taken on north-facing (in yellow), east-facing (in blue), south-facing (in purple) and west-facing (in red) slopes in Palikir Crater. Pixels have respectively the following orientations: 340°, 81°, 160° and 265°. Slopes are similar, respectively 19.6°, 20.8°, 21.8° and 21.7°. C) Maximum insolation per day on the considered pixels.

where k is expressed in W m^{-1} K^{-1}, ρ is the density in kg m^{-3}, c is the thermal capacity in J kg^{-1} K^{-1}. Thermal Inertia Unit (tiu) is J m^{-2} K^{-1} s$^{-1/2}$. For clarity, we will use the designation of tiu from Putzig, 2006 to express the thermal inertia units. Thermal inertia has already been defined at the global scale using THEMIS data by Ojha et al., 2014 and we fixed its value to 400 tiu for a dry surface. This value correspond to the one found by THEMIS at the RSL locations. Apparent thermal inertia depends on several independent parameters (Putzig, 2006), such as slopes and azimuths, surface heterogeneities, seasons or local hours. It also depends on temperatures, as it is a function of the medium conductivity k, which depends itself on temperatures (Piqueux and Christensen, 2011). Fixing the thermal inertia in our model allow us to focus on the topography effects on the solar flux. Tests with thermal inertia fixed at 250 tiu have been performed, yielding to a seasonal surface temperatures' global shift to higher values. Variations of seasonal temperature remain unchanged.

Another important parameter is the Bond albedo which controls the amount of absorbed solar flux at surface. The mean bolometric albedo on Mars is 0.25 (e.g. Christensen et al., 2001) but darker areas like on RSL sites have lower values, typically around 0.10 (e.g. Stillman et al., 2017). Hence, we used a bolometric albedo $A_B = 0.10$ to model the surface where RSL occur. In our model, bolometric albedo rises automatically to 0.65 when computed temperatures reach 149 K, that corresponds to the CO_2 condensation temperature threshold, to model the effects of CO_2 ice at the surface.

Surface and bottom boundary conditions Energy balance at surface involves various incoming sources of energy such as insolation, atmospheric effects, latent heat of CO_2 as follow :

$$\frac{E_\odot}{d^2}(1 - A_B)\cos(i) + q_{atm} + L_{CO_2}\frac{dm_{CO_2}}{dt} = -k\frac{\partial T}{\partial z} + \epsilon\sigma T^4, \tag{6}$$

where $E_\odot$ is the solar constant ($E_\odot = 1368$ W.m^{-2}), A_B is the bolometric albedo, d is the distance to the sun in AU, q_{atm} is the part of the reemitted flux from the atmosphere (long-wavelength irradiance, set at 2% of noontime insolation, in W m^{-2}), L_{CO_2} is the latent heat in J kg^{-1}, k is the conductivity in W m^{-1} K^{-1}, ϵ is the surface emissivity (set equal to 1 in Kieffer's definition which corresponds to a black body) and T is the temperature in K. From left to right, terms in equation 6 are the expression of the insolation, atmospheric radiation, CO_2 condensation/sublimation transition, heat conduction and planetary surface reemission (figure 6).

Bottom boundary condition is the adiabatic condition

$$\frac{\partial T}{\partial z} = 0, \tag{7}$$

suggesting that there is no heat transfer through this boundary. The temperature at the base of layers is first set to the mean annual equilibrium temperature whose expression is :

$$T_{eq} = \left(\frac{E_\odot}{d^2}\frac{1 - A_B}{4\epsilon\sigma}\right)^{1/4}. \tag{8}$$

We choose T_{eq} as an input to initialize the layer temperatures. MarsTHERM uses the Newton's convergence method to find the surface temperature where differences between incoming flux and outgoing flux (equation 6 and figure 6) is below a given threshold ξ, close to zero. Here, ξ is set to 10^{-5}. This convergence criterion has been implemented in the original fortran code developed by Clifford and Bartels, 1986. We also added another convergence criterion to ensure the steady thermal state over the years for every pixel of our DEM to guarantee the convergence throughout the years. Indeed, the initial temperature we use can vary from the average temperature of our calculations area. We implement a criterion to check the differences between years for surface and subsurface temperatures for a same solar longitude L_S (angle defining the position of Mars on its orbit). The criterion is applied in an independent way on every pixel of the DEM, such as the number of years necessary to converge is adaptive from a pixel to another. The threshold has been adjusted to 10^{-4} for our calculations and is compared to the normalized temperature difference ΔT over two consecutive years.

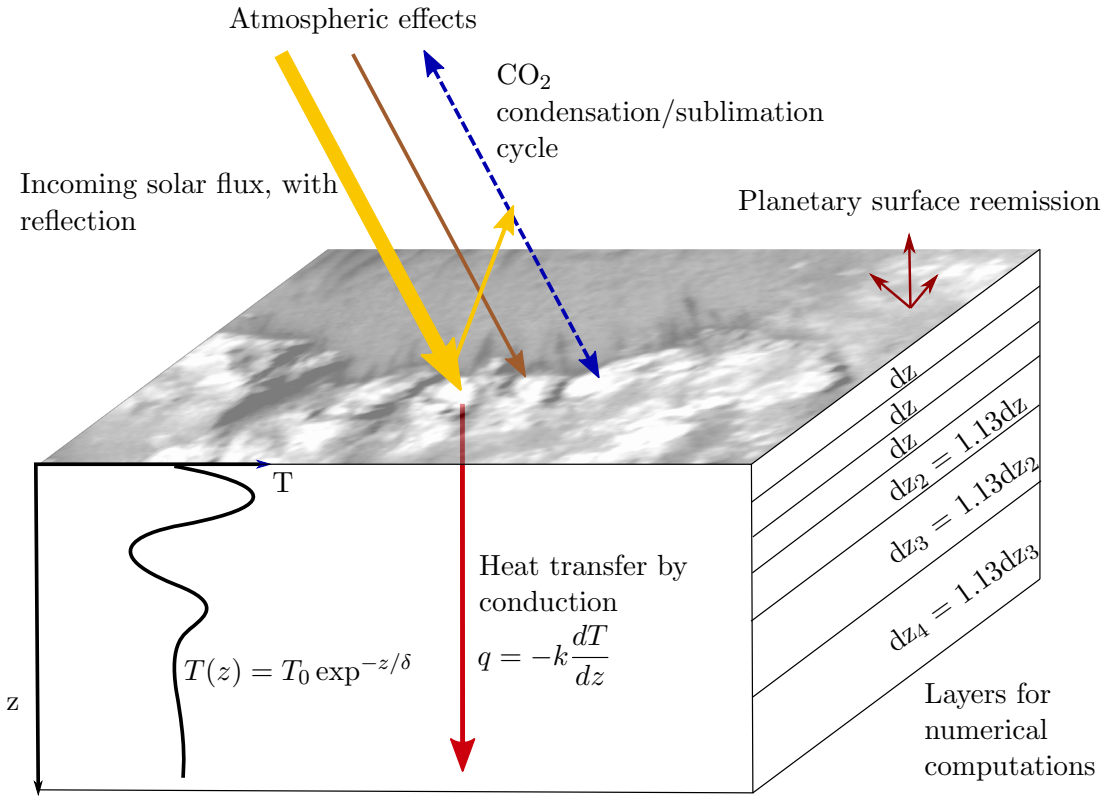

Figure 6: Scheme representing the different incoming and outgoing fluxes we take into account in our thermal model. Part of the insolation is reflected at the surface depending on albedo, while heat penetrates in ground as shown by the vertical temperature profile following the conduction law. Calculations are performed on different numerical layers to optimize computation time. Deepest subsurface layers have increasing thicknesses to optimize computation time, directly dependent on the top layer thickness.

Following the stability criteria defined in Clifford and Bartels (1986), we make the temperature computations on layers of increasing thicknesses with depth (figure 6). Stability criteria depends on physical parameters of the ground (e.g. thermal inertia) and the time step $\Delta t \sim 30$ min. The three first layers are defined with a thickness $dz \sim 2$ cm, then dz increases as $dz_i = 1.13 dz_{i-1}$ to minimize the computation time. In the end, the temperature profile reaches a few meters depth, for a maximum of 40 layers.

Thermal skin depth The depth at which heat transfer by conduction is efficient can be defined using the thermal skin depth. It depends on the period of the incoming energy oscillations. This thermal skin depth δ_{th} can be defined regarding diurnal or seasonal cycles. δ_{th} depends on I (tiu) and the period of oscillations P (in seconds, a sol for the diurnal cycle and a year for the seasonal cycle) such as

$$\delta_{th} = \frac{I}{\rho c}\sqrt{\frac{P}{\pi}}. \tag{9}$$

For a basaltic-andesitic crust, which corresponds to the general composition of the martian crust (Bandfield et al., 2000; Nimmo and Tanaka, 2005; Zuber, 2001), we can compute the corresponding δ_{th} for a sol and a year, respectively $\delta_{th}(\mathrm{P} = 1\ \mathrm{sol}) \sim 7$ cm and $\delta_{th}(\mathrm{P} = 1\ \mathrm{Y}) \sim 1.7$ m. Temperatures in shallowest layers are forced by both diurnal and seasonal cycles, while deepest layers are controlled by seasonal cycle. To achieve a good convergence and stability at the bottom layer, we compute heat

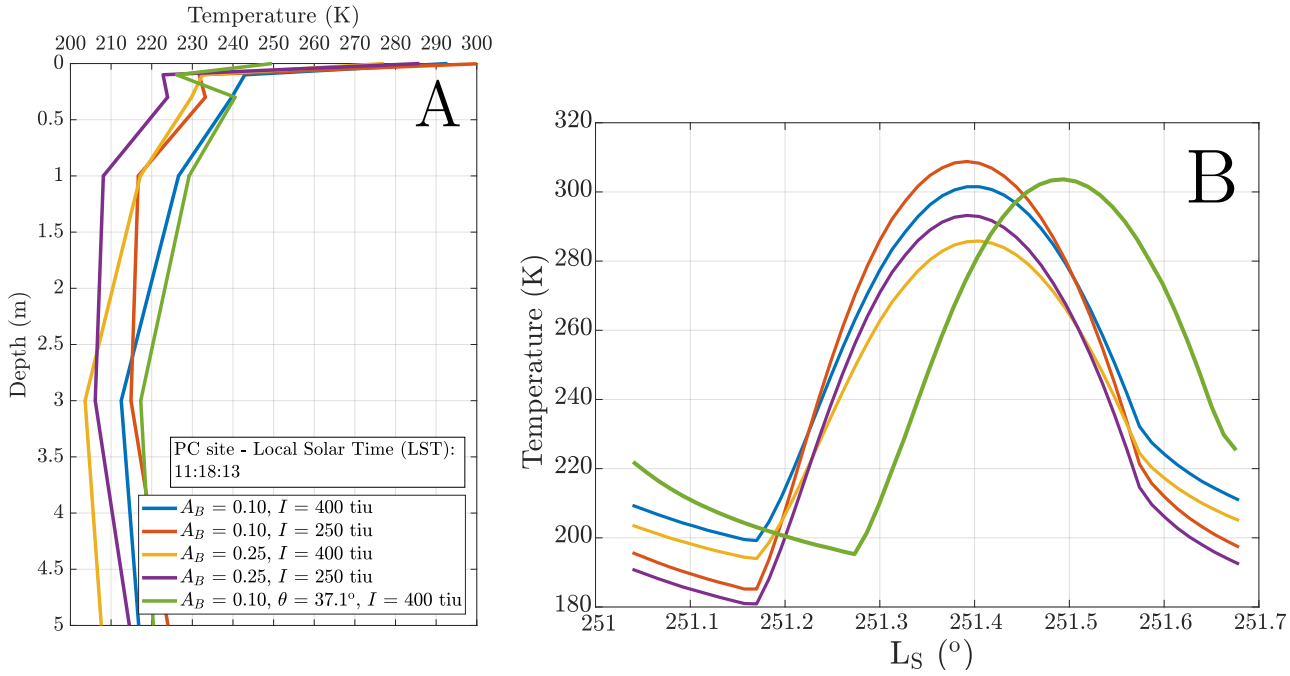

Figure 7: A) Temperature vertical profiles and B) surface temperature variations with time for a full day around $L_S \sim 251°$, located on a nearly flat surface (∼1°) east of PC site. Green temperature profile is located on a 37° sloped surface on eastern wall of Palikir crater, with a west-facing orientation. These plots are established for various couples of bolometric albedo (0.10 or 0.25) and thermal inertia (250 or 400 tiu).

transfer up to ∼3 seasonal thermal skin depth. Computations are performed up to five years before any use of the output to reach a stable state at the bottom.

From 1D temperature profile to temperature maps For each pixel of our DEM, surface and subsurface temperatures (from the surface to few meters depth) are then calculated according to the physical parameters we defined (thermal inertia, albedo). Figure 7A presents the vertical temperature profiles for several couples of bolometric albedo and thermal inertia with typical values of martian surface physical parameters, for flat (blue, red, purple and yellow profiles) and sloped surfaces (green profile). A_B has been set to 0.10 or 0.25, which corresponds respectively to albedo from dark terrains where RSL occur (e.g. Stillman et al., 2017) and mean martian albedo (Kieffer et al., 1977). These extreme values have been used to provide day and vertical profiles with significant temperature differences between them. I values are 250 or 400 tiu to model surface terrains with, for example, different grain sizes. In case of high thermal inertia, low amplitude thermal wave penetrates more deeply than for low thermal inertia where we observe shallow thermal wave of high amplitude (equation 9). Thus, highest noon surface temperatures are correlated with low thermal inertia. Daily temperature variations show (figure 7B) how surface temperatures are also affected by low bolometric albedo (= 0.10) for most of the day, increasing the temperature maxima by ∼ 20 K compared to higher albedo (= 0.25). Temperature daily profile for the sloped surface presents a time shift of around 4 hours (figure 7B), due to its west orientation. We then adapt MarsTHERM to input insolation tables computed with our insolation program. For each pixel, the program computes the temperature profile in depth direction. For each DEM, the output is a data cube (latitude, longitude, depth). Data cubes are produced for each time step to determine the temperatures of the martian surface and subsurface with a high temporal resolution (∼15 min).

2.4.3 Limitations and assumptions

The accuracy of the length measurements is limited to the HiRISE spatial resolution (∼25 cm/px,

McEwen et al., 2007). At least three pixels are needed to resolve an object, which is about one meter for each termination point of our length measurements. Hence, our measurements cannot be more precise than this resolution. In addition, despite the albedo contrast, RSL terminations are sometimes difficult to distinguish from surrounding terrains, adding some uncertainties to our measurements. Empirically, we have assumed a conservative error of 2 meters. In the end, our observations are limited by the temporal coverage of HiRISE images, which varies with locations. However, we limited this challenge by restricting our investigation to well-covered RSL sites, which present at least ten HiRISE images, so that each site is covered for at least two martian years.

Predicting martian's surfaces and subsurfaces temperatures on RSL sites required some assumptions. The thermal inertia has been fixed to 400 tiu which represents an average typical value on Mars for RSL sites (e.g. Ojha et al., 2014; Tebolt et al., 2020) for one of our calculation. RSL terrains contain few meters width boulders and some featureless smooth material such as sand or dust (Putzig, 2006). Most of the RSL features originate near massive boulders at the slope tops and terminate on more fine-grained surfaces. We can expect a spatial mixing of different thermal inertia compounds, but quantifying thermal properties heterogeneities is out of reach at the HiRISE pixel scale. However, our ROI are visually homogeneous enough so that assuming a single thermal inertia is reasonable. This method ensures that our results are not forced by our input: surface temperatures are only affected spatially by variations of insolation. Ideally, a thermal inertia map with a similar resolution than HiRISE camera would be required to include thermal inertia spatial variations. However, the best spatial resolution related to thermal inertia estimations is 100 m per pixel, that is too large to solve the RSL area. Effective thermal inertia can also been significantly affected by the presence of liquid water (Edwards and Piqueux, 2016; Piqueux and Christensen, 2011). Also, RSL may be either dry process (Dundas, 2020; Dundas et al., 2017b; Schmidt et al., 2017; Vincendon et al., 2019) or processes with limited concentration of 3%wt max (Edwards and Piqueux, 2016). ported in Tebolt et al., 2020's supplementary data are not significantly different from one site to another. For all these reasons, fixing the thermal inertia at 400 tiu is a reasonable approach for our study as a first approach for a dry model. We also make temperature computations using varying physical properties of the ground, including thermal inertia, to model the effect of RSL activity if we consider them as wet processes. Thermal flux due to scattering from dusty Martian's atmosphere $q_{\odot}$ (equation 6) is assumed to be a constant fraction of the solar insolation. Pixels in shadows receive no direct insolation, thus no scattering flux. Seasonal temperature profile within RSL ROI may not be significantly modified as pixels are almost all illuminated at HiRISE LST. We also neglect the local effects of dust opacity or pressure variations on the radiative transfer through atmosphere as small-scale variations are difficult to estimate and Mars GCM models are restricted to larger scales (e.g. Madeleine et al., 2011). Heat exchanges between soil and atmosphere is anyhow negligible for most of cases on Mars (e.g. Spiga et al., 2011; Sutton et al., 1978), and the uncertainties on the albedo may affect our results much more. Bolometric albedo has been set to 0.10, which is an intermediate value between dark RSL (0.09, Stillman et al., 2017) and regional dark areas where RSL occur (∼0.15, Stillman et al., 2017). Thus, Mars atmosphere is considered completely homogeneous. We do not take into account local shadowing due to small-scale topography. Local shadowing by neighboring topography may imply sunrise and sunset local time variations (Schorghofer et al., 2019). Surface temperatures would decrease close to RSL tops, due to the boulders' shadows, on few pixels near the ROI top boundary. Changes on seasonal temperature profiles remain negligible, as profile values are average surface temperatures within the ROI, besides, our seasonal temperature profile for PC site is in good agreement with Schorghofer et al., 2019's temperature profile for $I = 400$ tiu (see their figure 1). Finally, as we study local topography, we pay attention to the errors on slopes estimation. Slopes are computed using the HiRISE DEM with the nine neighbors pixels, thus the errors on slopes directly depend on the vertical precision of the DEM. Digital elevation models created from HiRISE data show a vertical accuracy of < 0.5 meter (Kirk et al., 2008; Sutton et al., 2015). Thus, a local slope estimated to $S = 30°$ between two neighbor surface elements, imply an error on insolation less around 4-5°(Millot et al., 2020, ∼13.3-16.7%) at first order. This value is in agreement with our standard deviation results summarized within section 3.2.

3 Results

3.1 Characterization of the RSL seasonal activities

We measure the RSL activity from three RSL sites located at different latitudes, (that includes 4 ROI: 1 for PC and 1 for RC, 2 for CC with NW and SW orientations), as mentioned in section 2. CC site displays numerous RSL features on Valles Marineris southern walls, occurring mainly on north to west-facing slopes, but several northeast and southwest-facing RSL are also visible. In PC site - which is part of well-studied Southern Mid Latitudes (SML) sites (e.g. Stillman and Grimm, 2018) - RSL are located on eastern part of Palikir crater, with northwest and west-facing lineae. RC site shows RSL on west-facing slopes of Rauna Crater. We refer the reader to the supplementary material and figure 9 for a complete description of the RSL activities. To complete this morphological description, we measure RSL lengths using HiRISE images up until MY 34 ($L_S = 113.3°$) and MY33 ($L_S = 79.6°$), respectively for NW and SW-facing RSL in CC site, MY31 ($L_S = 349.3°$) for PC site and MY32 ($L_S = 343.2°$) for RC site. An RSL length estimation consists on averaging several lineae lengths measurements on a given RSL site 3. This is used to characterize the activity. Length measurements are performed on a single RSL area per site (excepted for CC site, which is detailed below), represented in figure 1A-D, based on the local albedo variations. The number of recurrent lineae targeted is specified in table 1 as number of measurements.

Whereas we focus on a single RSL area for our thermal study in PC and RC sites, we study two distinct zones in Coprates Chasma (figure 8A), each zone displaying different preferential RSL orientations (SW and NW, figure 8A and table 1). CC (SW) site shows SW-facing RSL (figure 1B and close-up on figure 8A) which has been used to make our thermal modeling (figure 13) and geomorphological study (figure 9, and supplementary data). As an exception, two NW-facing RSL areas have been studied in CC (NW) site (figure 8A and B). Smallest RSL area, in northern part of the HiRISE image (figure 8C), is used for lineae length profile summarized in figure 9 and geomorphological descriptions in supplementary data, as well as thermal modeling in figure 13. Close-up highlighting the ROI, which is used to make the temperature computations, is represented in figure 8C. Largest RSL area, in southern part of the image from 8B, has been used to provide elevation and insolation profiles (figures 10 and 12), as well as insolation maps (figure 11), in order to discuss about the interactions between small scale topographies and insolation.

RSL site (orientation)	Locations	Mean slopes (°)	# of measurements	# of images
PC (NW)	41.6°S, 202.3°E	37.3	9	27
CC (NW)	13.0°S, 295.5°E	28.6	10	12
CC (SW)	12.6°S, 294.7°E	34.0	10	14
RC (W)	35.2°N, 327.9°E	30.6	9	23

Table 1: Summary of studied RSL sites parameters, with locations in geographic coordinates, mean slopes, number of length measurements and HiRISE images.

Figure 9 represents the mean length profiles provided by lineae length measurements towards slope direction. Both CC and PC sites has HiRISE coverage for four consecutive MY. CC profiles present the effects of slope orientations for two different RSL areas, with a northwest (9A) and southwest (9B) orientations. Mean slopes are similar (respectively 34.0° and 28.6°) as well as geographical coordinates. Indeed, both sites are located on subequatorial RSL sites at comparable longitudes (12.6°S, 294.7 °E and 13.0°S, 295.4°E). The orientation is the only geometrical parameter presenting a significant variation with ∼225° and ∼320°, respectively for SW-facing and NW-facing RSL. Length profiles are then noticeably different, NW RSL displaying highest lengths over the year during L_S = 90-140° while SW RSL lengths are the lowest around $L_S = 90°$. SW RSL activity is particularly visible in figure 9B, since HiRISE images cover a wide range of solar longitudes for MY32. PC site highlights long period of time without any RSL activity during southern winter, from $L_S \sim 30°$ until $L_S \sim 250°$. Around perihelion, lineae lengthen from few meters to reach 180 meters long and continuously fade from $L_S \sim 310°$ to disappear around 30°. RC profiles emphasizes a nearly reverse activity showing

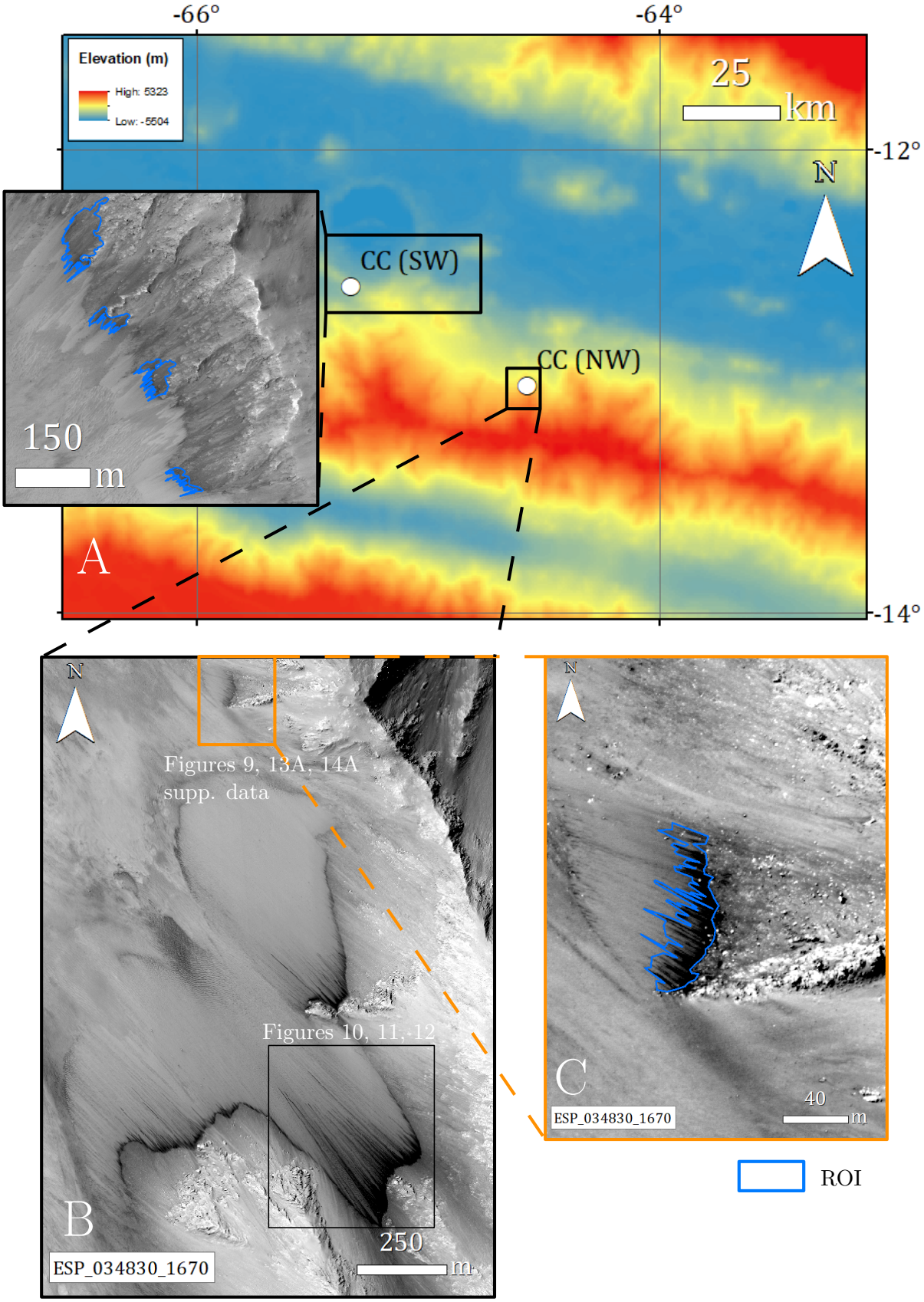

Figure 8: A) RSL regions in CC site on which we focus in the present study. Background is MOLA. Western region shows SW-facing RSL while eastern region presents NW-facing RSL. B) Close-up on CC (NW) region, where two RSL areas have been used in our study. C) Emphasis on the smallest RSL area on the right part of the figure, with a W-NW orientation. ROI contours are represented by the blue solid line. HiRISE image is ESP_032206_1675 for close-up in A and ESP_034830_1670 for B and C.

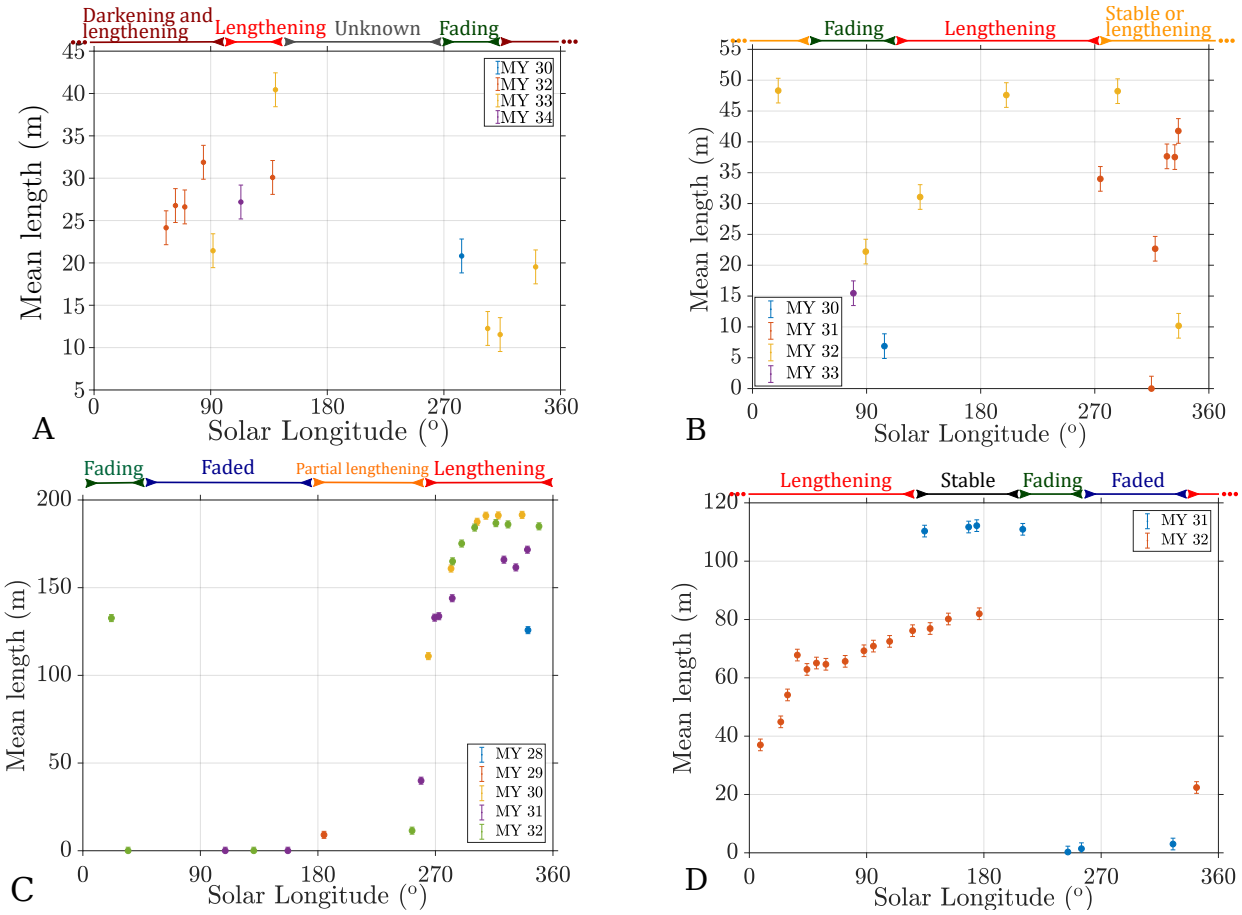

Figure 9: RSL mean lengths profiles for NW-facing and SW-facing CC (respectively A and B), PC (C) and RC (D) RSL sites. HiRISE coverage extends from MY28 to MY34, depending on the site. Lineae lengths are strongly influenced by latitude and slope orientations. Displayed error bars are a function of HiRISE images spatial resolution. As metric objects can be solved with HiRISE, we use a 1 meter spatial error for RSL length. The activity is described for each RSL site: lengthening is used when recurrent lineae grow without darkening, partial lengthening is used when lengthening happens for a single or a few lineae among the set, darkening is used when we can observe an increasing albedo contrast with the surrounding terrains, fading when the albedo contrast is decreasing, stable when two consecutive images show no difference in length or albedo contrast and faded when lineae are not visible anymore. Notice the absence of HiRISE image during a long period of time for A): hence, we mention the activity as unknown.

that RSL sizes rise from 330° to ∼ 215° of solar longitude, before a sharp decrease (especially for MY31) at $L_S \sim 250°$. Our observations are in good agreement with previous studies (Stillman et al., 2016 for RC site, supplementary information from Chojnacki et al., 2016 for CC sites and McEwen et al., 2011 and Stillman et al., 2014 for PC site). Uncertainties of our length measurements are due to image resolution (25 or 50 cm/pixel) and variations of illumination. We set error bars equal to 2 m. Variations of illumination is somewhat negligible, as RSL are most of the time highly contrasted with surrounding terrains.

3.2 Local topography

CC site shows particularly large RSL clusters (Chojnacki et al., 2016). Sometimes, RSL tracks impacts the local topography described by HiRISE DEM. This is the case for the RSL area presented in figure 10, where large dark lineae are visible on few hundred meters in width and length (10A). The associated DEM also highlights linear downslope grooves, from which we compute orientations (10C) to underline these small scale linear features. Contiguous variations in orientation from southwest to northeast part of the figure 10C are witnesses of parallel trenches, stretched along the slope direction. Channels are however hardly visible in the transverse topographic profile represented in 10B, which shows that these tracks are narrow features whose depths are probably in the same range than the DEM vertical errors. Vertical precision is expected to be lower than 0.5 m (e.g. Sutton et al., 2015) for HiRISE team's DEM. Hence, channels may not exceed few tenths of centimeters or one meter in depth. Regarding that these tracks are visible continuously in the slope direction on figure 10C and overlap the dark lineae in 9A, they are surely not due to DEM vertical uncertainties, even if this error is in the same range as the channel depth. The presence of these channels rises questions about the RSL occurrences: either RSL appear preferentially in previous existing channels or RSL create them by superficial erosion caused by flowing. We can hypothesize that RSL occur in these trenches and erode the underlying substrate which yields to deeper channels. In this case, these deeper channels and their local topography favour the RSL occurrence and so on. For now, no evidence of significant erosion is present in the data.

Hence, our observations highlight that channels and RSL are correlated. As channels are visible in HiRISE DEM, we use our thermal model to determine if channels are related to insolation variations induced by changing slopes and orientations; in addition, we aim to investigate how RSL and such hypothetic differential insolation can be linked. We estimated the heterogeneities of the coming solar flux at the beginning of the afternoon during late southern autumn on RSL described in figure 10. Our results are summarized on figure 11 and show three insolation maps at three LST, from 1.00 to 3.00 p.m. Colorscale indicates the solar flux arriving on the surface from 0 to 500 $W.m^{-2}$. F is the mean insolation and σ_F is the standard deviation overall pixels. Insolation heterogeneities increase with declining sun (thus with growing incidence angle) whereas mean insolation decreases. Lineae signals are visible on solar flux maps, especially for 3.00 p.m insolation map (11C), where linear patterns appear in lower-left part of the map, correlated with dark lineae from figure 10A. Thus, insolation differs between channels and what we will call "interchannels" (the area between two lineae for a RSL area) during mid-afternoon in winter by about 65 $W.m^{-2}$ around 1.00 p.m until 130 $W.m^{-2}$ at 3.00 p.m. These results are averaged values along channel and interchannel profiles. However, variability of these values is high: standard deviations are respectively 83 and 121 $W.m^{-2}$. Furthermore, self heating process which commonly occur within channels or valleys is not accounted for in this computation. Self heating process will tend to reduce the insolation difference between illuminated and shadowed opposite slopes, typically in grooves and incised valleys. Spiga and Forget, 2008's estimations for reflected part are very low (in the order of 1 $W.m^{-2}$) compared to other flux components (see their table 1) for 15°'s sloped surfaces, but may increase within grooves. However, channels we observe remain very poorly incised as they are hardly distinguishable from noise along the profile 10B, so self heating process may act as a minor process here. Figure 12 highlights how insolation between channels and interchannels varies with time. It represents the evolution of the two insolation profiles (white dashed lines on figure 10C) from sunrise to sunset. Insolation differences are the largest after sunrise when around 8.30 a.m (12C), channels receive on average ∼65 $W.m^{-2}$ more than interchannels or before sunset, around 5.00 p.m, when channels are less heated compared

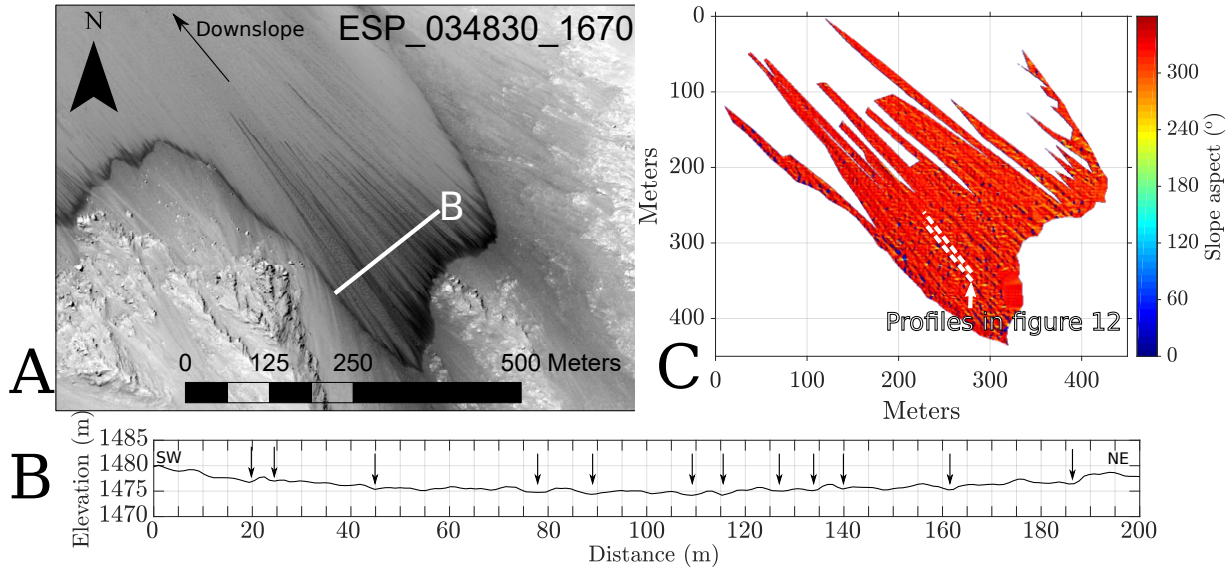

Figure 10: A) Large RSL in CC site. Lineae are few hundred meters long and are visible the entire year, with some shortening and lengthening phases. Downslope is northwest. White line is the trace of the topographic profile represented in B. B) Topographic profile of RSL area, normal to the steepest slope. Few channels are present and probably do not exceed few centimeters or few tenth of centimeters depth. Hence, they are hardly distinguishable from the possible noise due to DEM vertical precision. We underline the deepest channels by black arrows. C) Orientation map. Linear channels are present along the slope direction, underlined by consecutive variations in orientation values, particularly in the lower left part of the RSL area, where lineae are the largest.

to interchannels, with a difference in insolation equal to 170 W.m^{-2} (12F). Respectively, spatial standard deviations are ∼132 W.m^{-2} and 160 W.m^{-2}, which remains very high facing our results, due to HiRISE DEM vertical noise. However, facing the numerous linear patterns we see in figure 11C and their correlation with dark lineae, insolation differences are not random or resulting from data variability. Other linear profiles have been realized to furnish more estimations of the insolation at L_S = 0, 90 and 180°, providing similar insolation differences, with two spikes after sunrise and before sunset (see supplementary material). To summary, local topographies such as channels play a major role on insolation and by extension on surface temperatures which are significantly different between channels and interchannels in the early morning and in the late afternoon due to varying incoming flux in the energy balance.

3.3 Seasonal temperatures - Temperature maps

We assess mean surface temperatures for every RSL ROI. Eight temperature profiles among two different sets of parameters (a "dry" and a "wet" model) have been established from our temperature computations (figures 13 and 14) following the parameters values listed in table 2. We also add the maximum, mean and minimum temperatures for each day from one representative pixel (i.e. with similar slope and orientation than the ROI) to compare with the seasonal mean temperature of each ROI. Thermal inertia is first set at a constant value of I = 400 tiu to model dry surface or ground with a very low water content (figure 13), as suggested in Edwards and Piqueux, 2016. Then I and ρc are set to become variable to model the effects of a wet surface (5% water in volume), assuming a linear volume mixing (table 3) and with respect to RSL activity we reported (figure 14). Bolometric albedo is set to A_B = 0.10 for the results presented in figure 13. We also used A_B = 0.25 to see the effects of higher bolometric albedo on seasonal temperatures. The results of these computations are available in the supplementary material. Figure 13 shows temperature profiles for NW-facing (A) and SW-facing (B) slopes in CC site, PC site (C) and RC site (D), associated with spatial variances which provide an estimation of the surface temperature heterogeneities. Surface temperatures are more and more homogeneous as variance decreases. Solid lines are results for one pixel displaying close

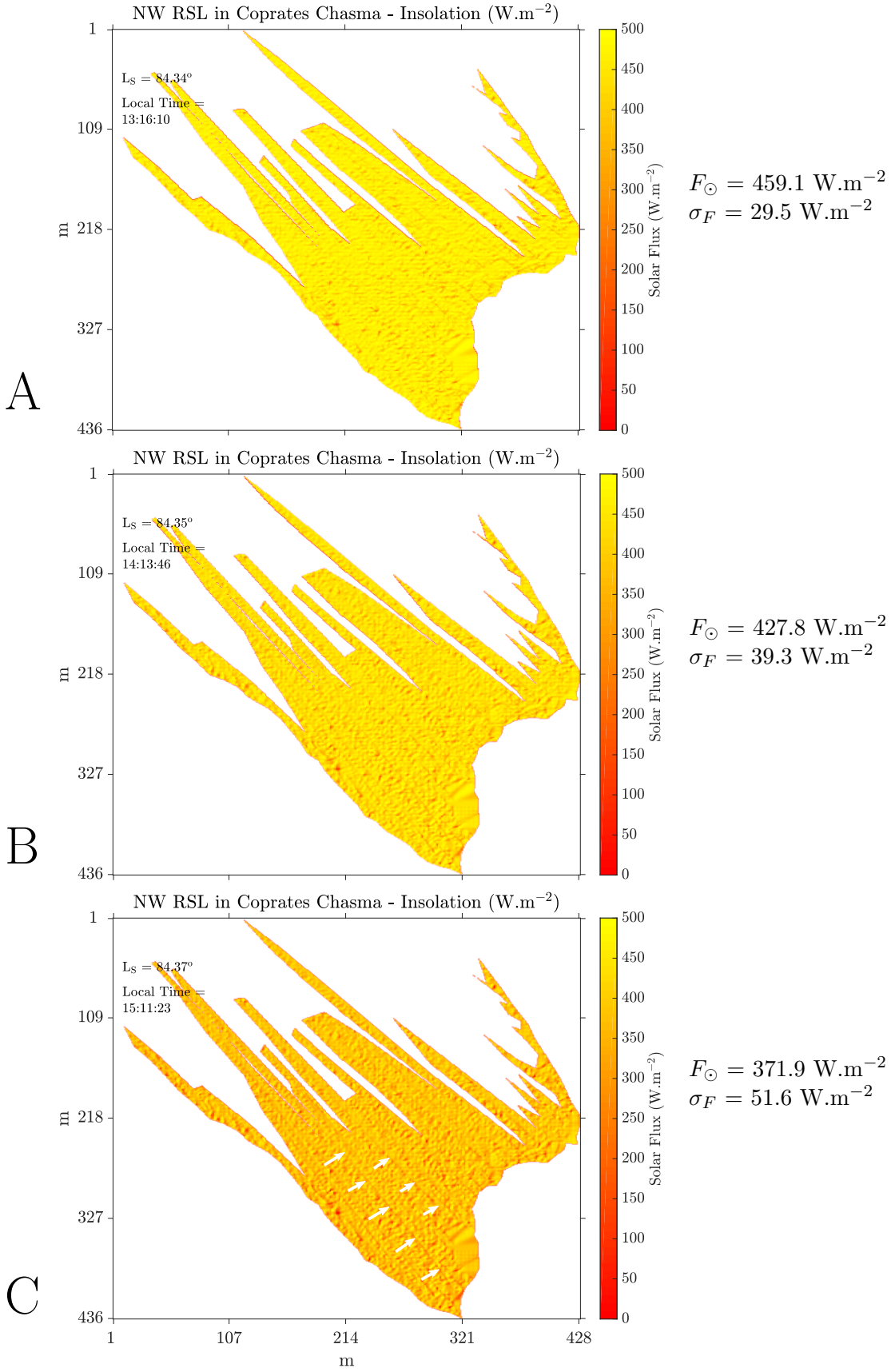

Figure 11: From A to C: insolation values on RSL area in CC site, from 1.00 p.m to 3.00 p.m LST, in W.m^{-2}, during southern late autumn. $F_\odot$ is the mean solar flux and σ_F the standard deviation overall pixels. Linear structures in insolation maps are due to the local topography and traduce the presence of the channels previously described (figure 10). σ_F is increasing as mean flux decreases, until sunset when insolation fall to zero. White arrows underline some channels in C.

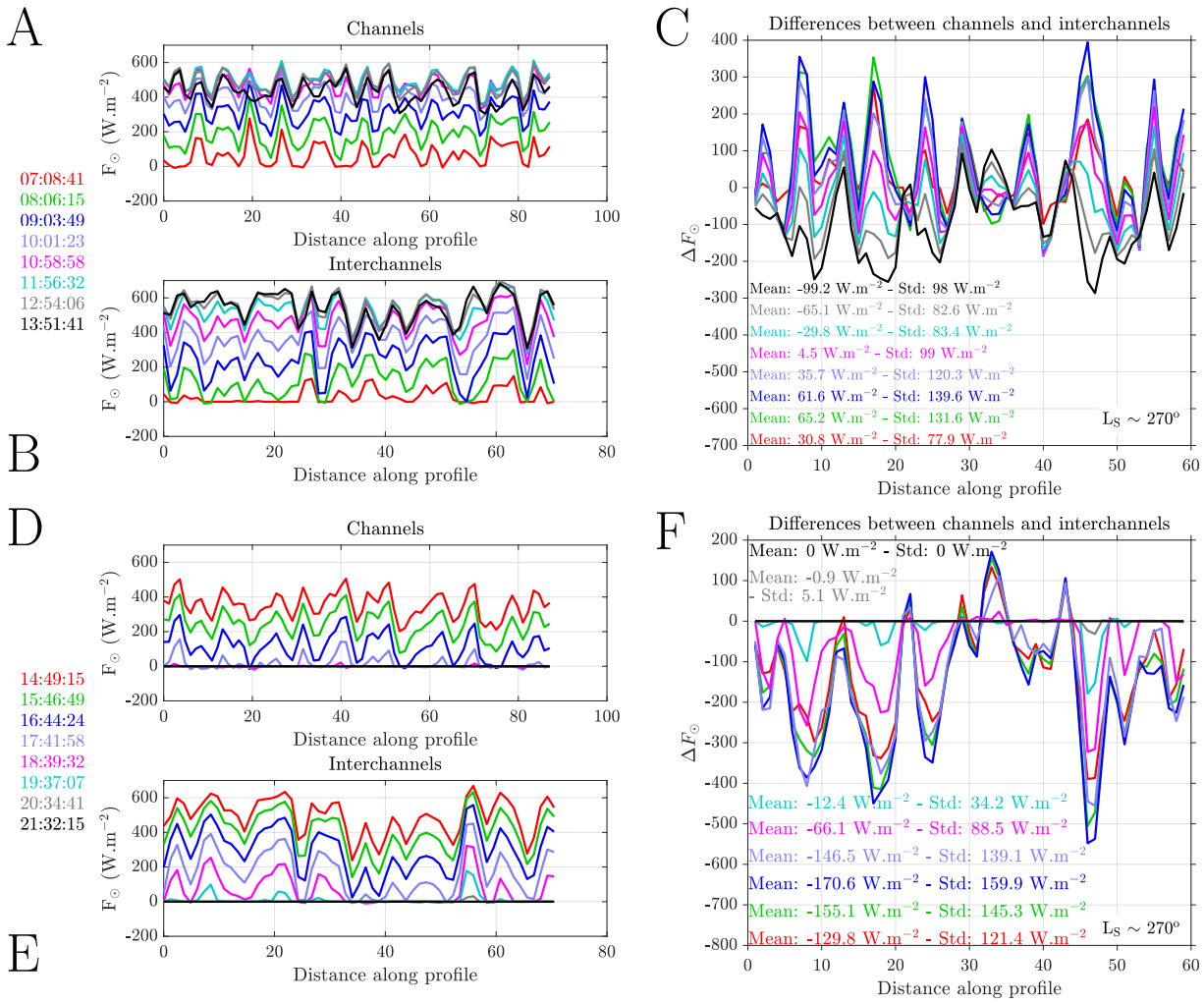

Figure 12: A) Insolation along a linear profile on a channel and B) on an interchannel on a RSL located in CC site, as represented in figure 10C, during the morning of the summer solstice (L_S = 270°). Profiles are derived from insolation maps as presented in figure 11. C) Differences between insolation profiles on a channel and an interchannel. Statistical descriptors are indicated on the lower left corner. Colorscale corresponds to LST. D) and E) are the same profiles than A) and B) during the afternoon of the summer solstice. F) Same than C) for the afternoon. Largest insolation differences between channels and interchannels appear before sunset, around 5.00 p.m.

Parameter	Symbol	Value	Unit
Bolometric albedo	A_B	0.10	∅
Thermal inertia	I	400 (figure 13) and see table 3	$J.m^{-2}.s^{-1/2}.K^{-1}$ or tiu (Putzig, 2006)
Equilibrium temperature	T_{eq}	~216.5	K
Emissivity	ϵ	1	∅
Boltzmann constant	σ	5.67×10^{-8}	$W.m^{-2}.K^{-4}$
Latent heat of condensation of CO_2	L_{CO_2}	5.9×10^{5}	$J.kg^{-1}$
Product of density and heat capacity	ρc	1004640 (figure 13) and see table 3	$J.m^{-3}.K^{-1}$

Table 2: Summary of parameters defined in MarsTHERM thermal model (Clifford and Bartels, 1986), with their name, symbol, value used for the presented calculations and unit.

orientation and slope values with mean ROI values. Black lines are temperatures extrema (maximum and minimum) for each during one year, and blue line is the average value per day. Equatorial sites (A and B, around 13°S) present similar surface temperature profiles throughout a year, with the lowest computed temperatures around southern winter solstice at $L_S = 90°$, and highest temperatures around southern summer solstice at $L_S = 270°$. NW facing-slopes profile (13A) show temperature limits at 259 K and 287 K, while maximum temperatures per day reach $\sim$ 295 K for NW-facing slopes around $L_S = 220°$ and decrease until $\sim$ 260 K in winter around $L_S = 90°$. SW-facing slopes display surface temperatures extending from 218 K to $\sim$ 295 K (13B). Around winter solstice, ROI average temperature slightly exceeds the maximum expected temperature for one pixel: respectively 218 K and 210 K. This is due to marginal pixel orientations (for instance N or NW-facing pixels whereas the global orientation is SW) within the ROI which tend to display reverse seasonal temperature profiles. This yields to lower seasonal variations for ROI seasonal profiles than expected for a single pixel profile. Maximum temperature for one pixel is similar to ROI's maximum temperature: 303 K around $L_S = 260°$. PC site (13C) and RC site (13D) are both located at mid-latitudes (41.6°S for PC and 35.2° N for RC). In PC site, average surface temperatures for ROI vary from $\sim$ 230 K at $L_S \sim 110°$ to 296 K around perihelion, at $L_S = 251°$, close to the southern summer solstice (at $L_S = 270°$). Maximum temperature per day presents similar variations, with a minimum at $L_S = 90°$ equal to 218 K and a maximum reaching 305 K around perihelion. Mid-latitude northern RC site displays a smaller temperature range from 253 K around northern aphelion ($L_S = 251°$) to reach 280 K at $L_S \sim$ 165-170°. Maximum expected temperatures per day ranges from 255 to 282 K (at $L_S \sim$ 275° and 160°), showing significant differences with ROI temperatures during winter and beginning of spring ($L_S \sim$ 270-360° and 0-30°). Hence, the widest ROI surface temperature ranges are displayed by SW-facing CC and PC sites, with a difference between temperature extrema ΔT of 77 K and 66 K, whereas NW-facing CC and RC sites present respectively $\Delta T = 28$ K and 27 K.

Figure 14 present the same temperature computations than figure 13, including varying thermal properties (thermal inertia I and product of density and heat capacity ρc) with respect to RSL reported activity and constraints on conductivity from Piqueux and Christensen, 2009. The input values for I and ρc are summarized in table 3, as well as L_S ranges. Low I and ρc values correspond to terrains where no RSL are present (dry surfaces); high values where RSL are active (wet surfaces). We choose to model a ground containing 5% of water in volume, to keep the granular flow behavior as previously observed (e.g. Dundas et al., 2017b). Globally, seasonal ranges of ROI temperatures

Thermal inertia (tiu)	400	400 → 1000	1000	1000 → 400
ρc (J.m^{-3}.K^{-1})	1004640	1004640 → 1455807	1455807	1455807 → 1004640
Rauna Crater	129.9-209.8°	209.8-244.4°	244.4-334.2°	334.2-129.9°
Coprates Chasma (NW)	293.8-327.1°	327.1-140.0°	140.0-211.9°	211.9-293.8°
Coprates Chasma (SW)	104.1-118.2°	118.2-200.2°	200.2-50.0°	50.0-104.1°
Palikir Crater	34.7-170.9°	170.9-340.5°	340.5-5.6°	5.6-34.7°

Table 3: I and ρc as a function of L_S, considering a linear volume mixing in transition phase, used as inputs in figure 14.

(blue dots) are preserved for both NW (14A) and SW (14B) CC sites, where temperatures vary from $\sim$ 250 to 280 K for the first and from 215 to 280 K for the second. Maximum temperature for one pixel exceeds 300 K $L_S = 210°$, which does not occur for "dry" (with constant thermal properties) case. PC site (14C) displays a lower ROI temperature range, from 235 around $L_S \sim 100°$ to 285 K around perihelion; however, maximum temperature profile considering one pixel (upper solid black line) remains comparable with one from figure 13C. Main changes come from RC site (14D) where ROI temperature profile remains quite stable (excepted around $L_S = 220°$, where sharp changes of thermal properties occur, see table 3): surface temperatures vary around 250-260 K as well as maximum temperature for one pixel, and no clear seasonality can be extracted from this ROI profile, neither from maximum temperature profile. Overall, every ROI temperature and maximum temperature for one pixel profiles present sharp discontinuities caused by changes of thermal properties.

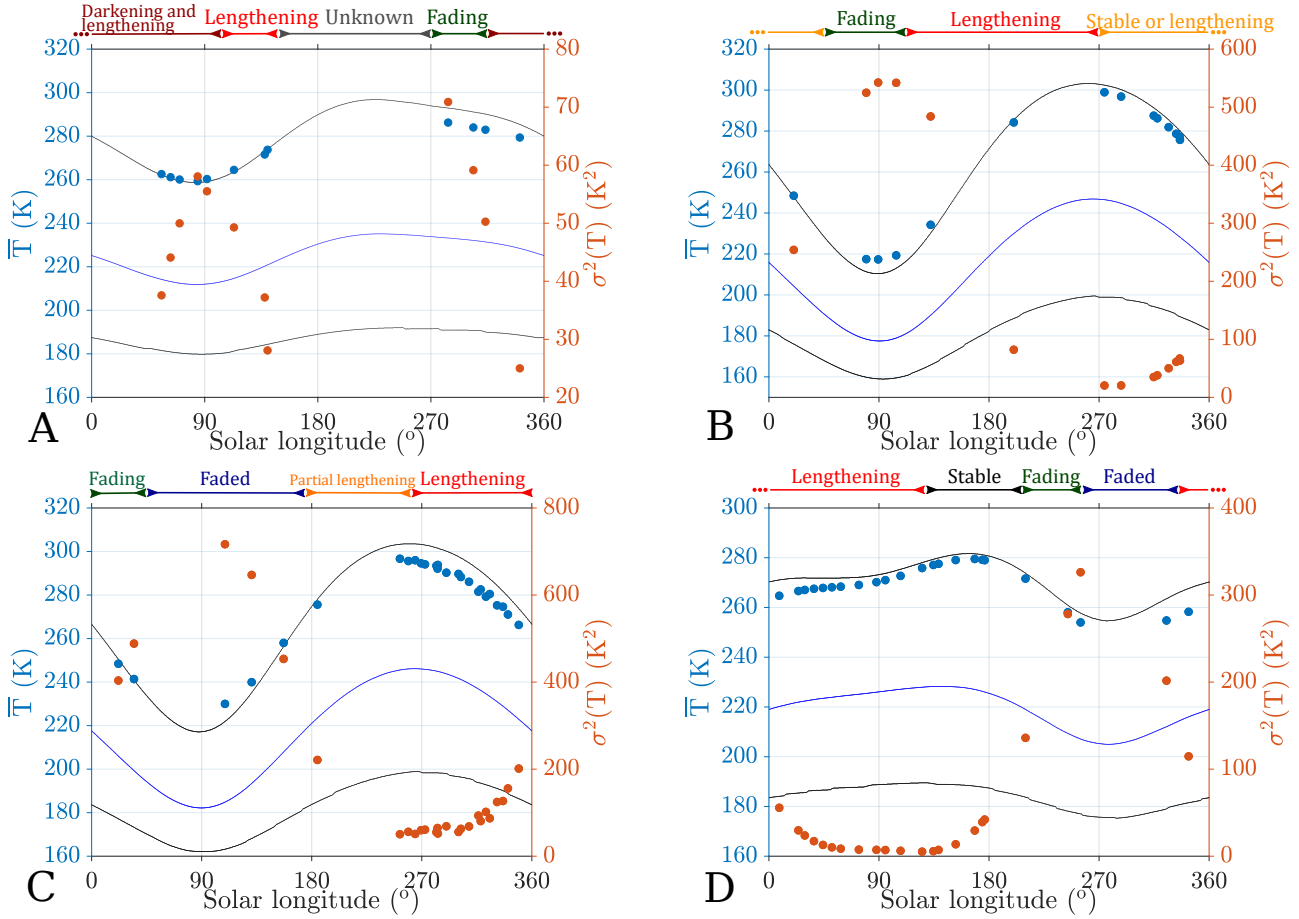

Figure 13: Average surface temperature for NW-facing and SW-facing CC (respectively A and B), PC (C) and RC (D) sites over the years (light blue dots) and surface temperature variance (red dots). Bolometric albedo is set to $A_B = 0.10$ and $I = 400$ tiu. Each point corresponds to the mean surface temperature computed for a solar longitude L_S at HiRISE LST, with an error in time $\sim$ 15 minutes. Solid black lines are temperatures extrema and blue solid line is the average temperature for each day for one pixel. The RSL description has been reported from figure 9.

Our results also emphasize the limited correlation between surface temperatures and RSL apparent activity. RSL lengthening is poorly linked with highest surface temperatures in the year for every RSL site for both computations, excepted for PC site where surface temperatures at HiRISE LST exceed 290 K for results in figure 13C and 280 K in figure 14C during RSL lengthening. It is also challenging to link RSL activity and temperature variations. For computations with constant I and ρc, lengthening times are associated by turns with successively decreasing and increasing temperatures for NW-facing CC (figure 13A), increasing temperatures for SW-facing CC (figure 13B), stable or decreasing temperatures for PC (figure 13C) and increasing temperatures for RC (figure 13D). Stillman et al., 2020 recently report how increasing temperatures are correlated with RSL lengthening activity. This trend is also observed in our results for three of our four computations, with an exception in PC site, where surface temperatures remain stable while lengthening occurs. It also appears that lengthening occurs before surface temperatures increase in NW-facing CC site, but this trend remains while temperatures increase. For the wet model, RSL lengthening times are similarly correlated with ROI temperatures variations compared to the dry model, excepted for RC site, where RSL activity is associated with decreasing temperatures during northern summer. We also produce temperature maps to further

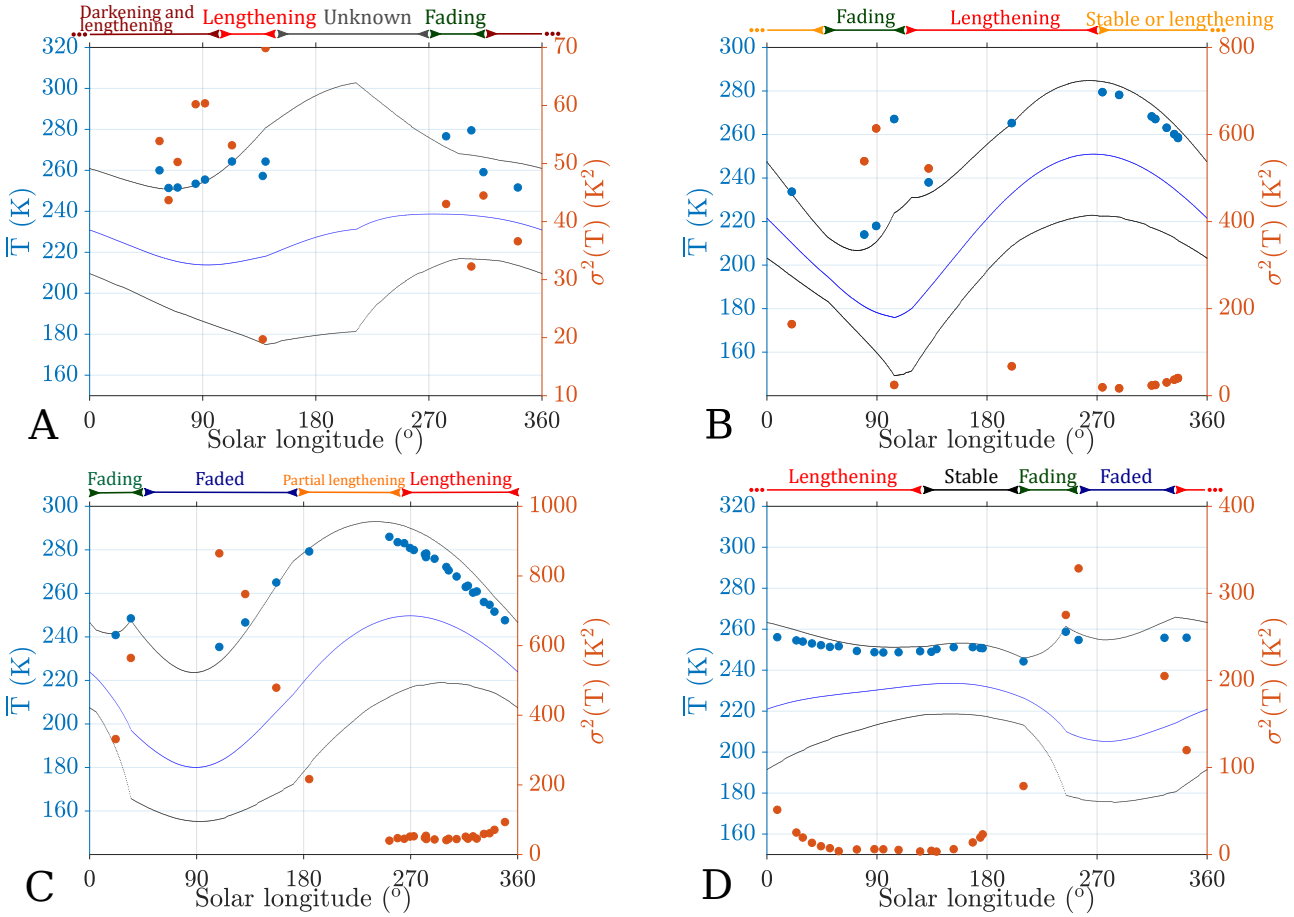

Figure 14: Average surface temperature for NW-facing and SW-facing CC (respectively A and B), PC (C) and RC (D) sites over the years (light blue dots) and surface temperature variance (red dots). Bolometric albedo is set to $A_B = 0.10$ and I linearly changes according to RSL reported activity between 400 tiu (dry surface) and 1000 tiu (wet surface). Each point corresponds to the mean surface temperature computed for a solar longitude L_S at HiRISE LST, with an error in time $\sim$ 15 minutes. Solid black lines are temperatures extrema and blue solid line is the average temperature for each day for one pixel. The RSL description has been reported from figure 9.

assess lateral temperature heterogeneities induced by differential insolation with the corresponding HiRISE images for RSL located in RC site (figure 15). The HiRISE images presented have been taken during northern winter ($L_S = 254.9°$) and summer ($L_S = 95.2°$). Surface temperature maps show differences in spatial temperature heterogeneities depending on the season. Winter temperature

maps (15B) display greater spatial temperature variations than for the summer map (15B'). We measure these temperature variations with standard deviations σ associated with their temperature histograms (figure 15C and C'). RSL in RC site is present when σ is minimum (σ = 2.7 K), at high and homogeneous surface temperatures during northern summer. On the contrary, σ is high (σ = 18.1 K) when temperatures are lower during winter and dark lineae are not visible. More generally, low lateral temperatures variations are most of the times associated with warm times and inversely (see figure 13B-D for instance). Maps have been computed at similar LST, around 3.00 p.m. to avoid the effect of diurnal cycle. Hence, surface temperature differences between 15B and 15B' results from the seasons, respectively winter and summer. In winter, sunrays reach the surface on average with a larger incidence angle than during summer, yielding to a lower insolation (see equation 4).

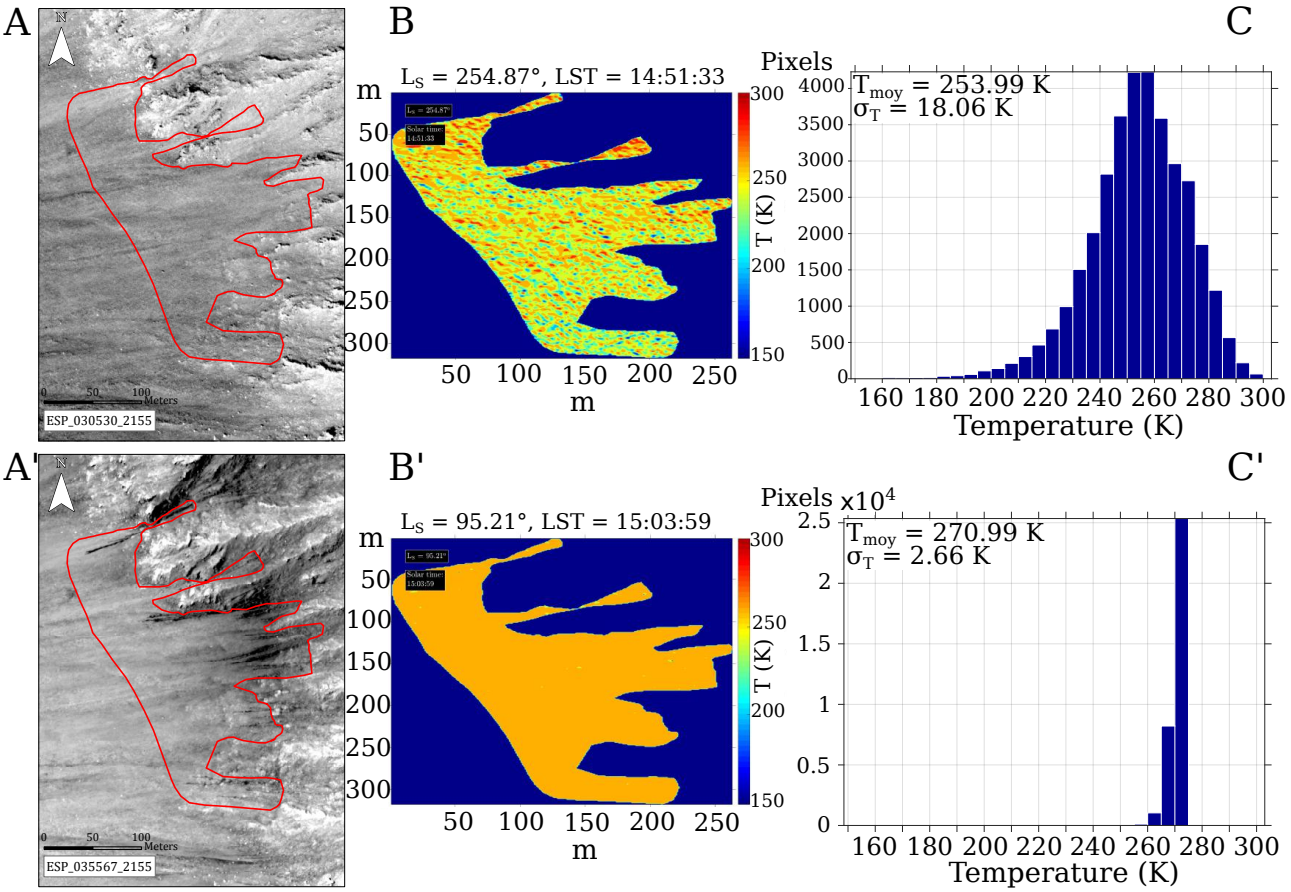

Figure 15: A and A') RSL area in RC site for HiRISE ESP_030530_2155 and ESP_035567_2155. The red area encompasses the zone of computations. B and B') Surface temperature maps at the same local hour and L_S than corresponding HiRISE images. Notice the differences in surface temperature variations. C and C') Histograms presenting the temperature distributions for both temperature maps. Mean and standard deviation are indicated on top left part of the plots.

Thermal models results are summarized in figure 16. Dry and wet models (respectively figures 13 and 14) are indicated, as well as our observations of RSL activity within RC, CC (NW), CC (SW) and PC sites. Plain bars are supposed RSL lengthening times, when maximum surface temperatures exceed the eutectic temperatures of different components. We consider three chemical species using eutectic temperatures from Chevrier and Rivera-Valentin, 2012's study: H_2O (T_E = 273 K), $MgSO_4$ (T_E = 268.6 K) and NaCl (T_E = 252.2 K). Generally, expected lengthening times for every component are poorly correlated with RSL reported activity, for dry model as well as wet model. Dry model is in good agreement with PC and CC (SW) RSL activity, respectively for water and NaCl: expected lengthening times range from $L_S \sim 180°$ to $L_S \sim 350°$ and from $L_S \sim 150$ to 20°. Wet models results show a lower fit with reported activity. For CC (NW) and RC sites, no expected lengthening time fits with reported lengthening time for the dry model. Therefore, the introduction of variable physical

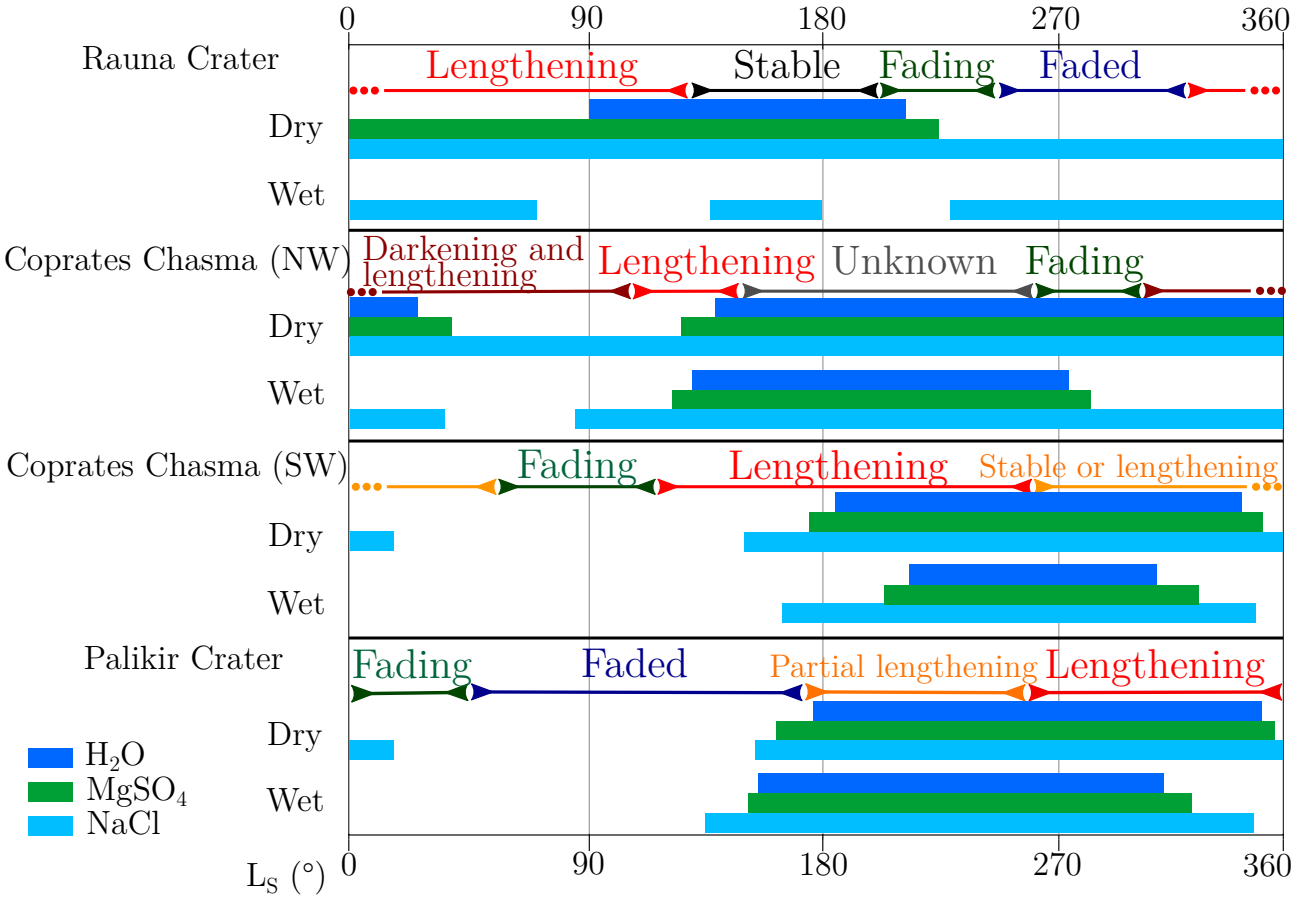

Figure 16: Longitude ranges for dry (i.e. with constant physical properties, figure 13) and wet (with variable thermal properties correlated with RSL activity, figure 14) models where daily maximum surface temperature exceeds different eutectic temperatures using values from Chevrier and Rivera-Valentin, 2012: H_2O (273 K, dark blue bars), $MgSO_4$ (268.6 K, green bars) and NaCl (252.2 K, light blue bars).

properties for the wet model implies substantial changes of expected lengthening for every species in RC and CC (NW) sites: we expect no RSL lengthening and reduced lengthening times for water and $MgSO_4$ in RC and CC (NW).

4 Discussion

4.1 Temperatures and RSL activity

Our calculations suggest that the amplitude of ROI temperatures variations are larger for SW orientations than NW orientations at equatorial latitudes, for both dry and wet models. This is related to season's asymmetry between north and south hemisphere, as southern summer and winter are respectively warmer and colder than northern ones, due to orbital forcing. Indeed, perihelion ($L_S = 251°$) is nearly in phase with southern solstice summer ($L_S = 270°$), and aphelion ($L_S = 71°$) with southern winter ($L_S = 90°$). Hence, north-facing slopes display surface temperatures following northern seasonality, with low contrasted seasons, while south-facing slopes follow southern seasonality with high contrasted seasons. However, for NW-facing CC site, lowest temperatures are found around $L_S \sim 80°$, which is similar to variations expected for southern seasonality. However, as pointed out by Stillman et al., 2020 for insolation, ROI surface temperatures remain relatively moderate for NW-facing site, which may be due to external forcing by orbital eccentricity. For dry model, it yields to some hybrid seasonality for the NW-facing slopes, with low temperature variations over a year similar to northern seasonality with a minimum around aphelion and a maximum at perihelion. This result is consistent with other studies at comparable latitudes (McEwen et al., 2014, their figure 4 for temperatures; Stillman et al., 2020, their figure 6 for insolation) in Garni Crater, at 11.5°S. For wet model, CC (NW) ROI temperatures remain relatively constant, but expected maximum temperatures show a minimum around 80° and a maximum at 220°, which is consistent with dry model. Surface temperature ranges are very different from a site to another for dry and wet models. RSL in PC site lengthen when ROI surface temperatures exceed 290 K for dry model and 285 K for wet model, whereas RSL lengthening is visible in SW-facing CC when temperatures are ~235 K for dry model and 240 K for wet model. Decorrelation is also observed during fading times. CC RSL is fading around 280-285 K for NW-facing slopes and < 220 K for SW-facing slopes for both models. Such differences in the temperature ranges within RSL lengthen or fade imply that the mechanism is not triggered at a universal temperature threshold. Physical properties changes induced by wet flowing implemented in the wet model do not solve the problem of ROI temperatures discrepancies between all the sites. In other words, RSL are either created by several different processes (linked or not to surface temperatures) or by a single mechanism, at least partially independent of the surface temperatures. Results presented here does not take into account the effect of varying atmosphere dust opacity, which yield to differences in scattering flux during a year. Regarding the data presented in Szwast et al., 2006 (their figure 1), seasonal increase in zonal mean dust opacity is correlated with increase in the atmosphere temperature of around 10-15 K and a surface temperature decrease of the same order. The temperature variations induced by this effect are higher for southern hemisphere. Hence, the most affected RSL site may be PC as it is part of SML sites. However, seasonality of the PC temperature profiles for dry and wet models may not be substantially modified with this order of temperature changes: southern winter and summer would remain the coldest and warmest periods of the year, with lower seasonal variations.

4.2 Discussion about previously proposed mechanisms

Regarding the wet hypothesis, the RSL reported activity may be linked to brines with distinct compositions at different sites (Chevrier and Rivera-Valentin, 2012). But such hypothesis cannot explain why global RSL lengthening starts when temperatures are greater than 280-290 K in PC ROI for dry and wet models, as this temperature far exceeds the melting point of pure water, even if a partial lengthening is reported around $L_S = 180°$. Considering the dry (or poor water content that does not affect significantly the thermal properties of the surface) model, water and NaCl are favored to flow in agreement with the reported activity within PC and CC (SW). These correlations decrease with

the wet model. Also, darkening is often interpreted as brine seepages (e.g. McEwen et al., 2014), resulting from underlying flowing water. However, seasonal temperature variations between RSL sites are different: finding a constant melting temperature suggesting one type of brine remains challenging. Moreover, water has not been detected on RSL sites for now (Ojha et al., 2013). Hence, our observations suggest ruling out temperature-dependent hypotheses such as water ice melting process (e.g. McEwen et al., 2011), or brines formation (e.g. Chevrier and Rivera-Valentin, 2012).

A recent study from Abotalib and Heggy, 2019 suggests that liquid water ascends along fractures from deep aquifers in highly deformed terrains to produce seepages at the surface (Gaidos, 2001). This statement is based on geomorphological study of Palikir crater, showing that RSL originate near concentric and radial fractures intersections in this area. Their models predict the presence of liquid water near the surface (< 1 km). Brines ascend along the fractures due to their higher hydraulic conductivity, seeping at the surface when temperatures are high enough to allow it. When temperatures fall, the artesian waters freeze within fractures until temperature increases above the melting point of brines. Highest surface temperatures are not correlated with periods of incremental lengthening for at least the two orientations in CC site in our study (figure 13A and B) for dry model, and in RC and CC (NW) for wet model (figure 14A and D), which is not consistent with thermal properties requirements for such mechanism. Yet, recent studies using neutron spectrometer to detect rich-hydrogen content conclude that aquifers distribution on Mars is poorly correlated with RSL locations (Wilson et al., 2018), even for well-correlated mid-latitudes site (PC). These results do not exclude the presence of aquifers smaller than the neutron spectrometer resolution (5°, Feldman et al., 2004a); besides, neutron spectrometer is only able to detect shallowest aquifers, up to few tenths of centimeters depth (Feldman et al., 2004a). Also, this mechanism does not explain why RSL are more present on west-facing slopes than east-facing ones (Stillman et al., 2017, their figure 12).

Another previously suggested interpretation was the deliquescence of salts (from solid to liquid state by adsorption of atmospheric moisture) such as perchlorates (e.g. Gough et al., 2014). Flowing would occur when the atmospheric RH outreaches DRH and flows as long as the RH is above the Efflorescence (from liquid state to solid state) Relative Humidity (ERH), when the salt starts to crystallize again. Due to hysteresis effect, the ERH necessary to recover the solid state is lower than DRH for calcium chlorides (Gough et al., 2016), hydrated sodium and magnesium perchlorates (Gough et al., 2014). DRH decreases with increasing temperature for calcium chlorides species (Gough et al., 2016), facilitating salts deliquescence with high temperatures. This hypothesis may explain at first order the correlation between high temperatures and RSL activity, but further assessments need to be done to evaluate the RH variations at RSL locations. RH has been measured seasonally by the instrument REMS boarded on the Curiosity rover (Martín-Torres et al., 2015) in Gale Crater (4.6°S, 137.4°E). REMS provides measurements of RH seasonal variations in the atmosphere (Martín-Torres et al., 2015). Highest RH values are present during southern winter and lowest in summer for both data, which highlights the good correlation between them. However, these measurements are quite difficult to reconcile to our reported RSL activities at similar latitudes (CC site, figure 1), as the lineae lengths variations depend on the slope orientations (figure 9A and B). Considering the atmospheric origin of moisture, it seems quite peculiar that opposite slopes do not exhibit RSL lengthening or fading at the same time. This argument has to be moderated as RH depends on temperatures, which significantly varies spatially due to insolation differences. Another issue to deliquescence process as a triggering mechanism is the RSL distribution, exclusively observed on low-albedo areas (e.g. Stillman, 2018). Even if low-albedo slopes facilitate warmer surfaces and subsurfaces (see equation 6), computed temperatures using a higher bolometric albedo ($A_B = 0.25$) are in the correct temperature ranges for perchlorates experiments conducted by Gough et al., 2011, 2014, 2016. Hence, ground temperatures are not a limiting factor on brighter slopes and reasonable DRH values are also reachable - typically few tenth % RH for chlorides hydrates (Gough et al., 2016), which is in the order of REMs measurements (Martín-Torres et al., 2015).

Thermal observations using THEMIS camera (Christensen et al., 2001) highlight the limited role of water in RSL (Edwards and Piqueux, 2016, less than 3%wt) and limited content of water available on Mars (Chojnacki et al., 2016) yields to dry hypotheses to explain RSL formation. Associated with the lack of water spectral detections, dry or hybrid processes become more and more studied. First,

dry flows induced by boiling water has been proposed (Massé et al., 2016; Raack et al., 2017) to explain RSL formation. Dry transport is triggered by underlying boiling water, ejecting fine-grained material downslope. Experimental studies reproduce successfully this mechanism (Massé et al., 2016; Raack et al., 2017). However, high temperature (> 273 K) are necessary to produce flows in their experiments, which is not consistent with our ROI seasonal temperatures in dry and wet models, excepted for PC site (figure 13C, 14D and 16).

A completely dry hypothesis has been advanced by Schmidt et al., 2017 involving Knudsen pump mechanism (De Beule et al., 2014). Knudsen pump induces gas-triggered flow under low pressures after the inversion of temperature vertical gradient caused by sudden shadowing of the surface (enhanced pump, Schmidt et al., 2017). Hence, shadowing occurs on top of steep slopes due to massive boulders, yielding to dry flow after few minutes. Due to the coarse vertical resolution of our thermal model, we are not able to determine if the gradient inversion occur in the first mm of the subsurface, but each site displays important temperature variations between the surface and subsurface (see figures in supplementary material), which is also the case at Garni Crater (Schmidt et al., 2017). The results from Schmidt et al., 2017 well reproduce the observed seasonality in Garni Crater at least for north-facing and east-facing slopes (Stillman, 2018) but further studies may be performed to determine if this dry mechanism explain other RSL seasonal activities. Nevertheless, this hypothesis is attractive as water is not necessary to explain the RSL activity. On the other hand, shadowing does, or at least sudden temperature gradient inversion. Dark streaks sharing some RSL characteristics (incremental lengthening and seasonal behavior) have been observed on sand dunes, on top of which boulders are not present to create shadows (Dundas et al., 2017a). Also, RSL do not necessarily originate on base of boulders as some have been described occurring on the middle of the slopes in Juventae Chasma (see Vincendon et al., 2019, their figure 10). Hence, shadowing is not necessary to produce this kind of granular flows. At last, recent observations of enhanced RSL activity after MY34 global dust storm (McEwen et al., 2019) highlight the link between them. As pointed out by Vincendon et al., 2019, shadows are reduced during dust storms due to increased atmospheric scattering, which is inconsistent with reinforced RSL activity if we consider Knudsen pump as a triggering process.

The fact that RSL sites are concentrated on low-albedo regions (e.g. Stillman, 2018) demonstrates the importance of this parameter, even if no instrument is able to estimate albedo changes at RSL scale, particular on steep slopes. Lower albedo are well correlated with poor dust coverage and may imply a more efficient heating at the surface (the reflected part of insolation is more important with higher albedo) (Szwast et al., 2006). In addition, it has been shown that these low dust coverage corresponds to transition zones between dark (i.e. no dust)/bright (i.e. high dust coverage) areas (Vincendon et al., 2019). Thin dust layer is then more easily removable to reveal underlying darker material. Albedo changes due to removal and deposition of dust by seasonal winds have been observed since the beginning of martian orbiters (Pollack and Sagan, 1967; Rea, 1964). More recent studies assess albedo changes with dust deposition after global dust storms (Szwast et al., 2006), while increased RSL activities are visible during seasons consecutive to Mars dust storms (e.g. McEwen et al., 2019). Hence, a close link between dust cycle and RSL activity is established. This dependency rises hypothesis involving that RSL are controlled by wind circulation and dust deposition/removal cycle over seasons (Vincendon et al., 2019). Dark lineae are then formed by dust removal by regional and local winds on steep slopes, revealing underlying darker substrate. This mechanism has several advantages, as it gets rid of temperatures direct dependency, do not necessarily involve wet flows of any kind and explain why the RSL activity timing is different with various orientations on equatorial sites.

At larger spatial scales, RSL sites distribution recently updated in Stillman, 2018 and wind streaks mapped by Thomas et al., 1981 are in good agreement. RSL sites are located in particular on dark erosional streaks areas which are created by surface erosion of dust coverage on darker substrate (Thomas et al., 1981). RSL are then small scale expressions of regional or global wind circulation, localized on steep slopes where winds can reach high velocities (Savijärvi and Siili, 1993; Spiga et al., 2011), fading during dust deposition or storms and flowing again when local winds are sufficient to produce dusty surface erosion. Hence, further studies must be performed to provide estimations of local slope wind circulation to decipher if this process is suitable for RSL.

5 Conclusion

RSL activity assessments through lineae length measurements and their thermal behavior have been compared in order to decipher which mechanism is consistent with our observations. We make length measurements at the best resolution we have using HiRISE imagery and their companion DEM for four sites on Mars, including equatorial and mid-latitudes sites for both hemisphere. We determine insolation and temperature variations using dry and wet thermal models which integrates SPICE/NAIF libraries to provide high precision calculations and large adaptability in order to question previously proposed RSL triggering mechanisms (table 4). Hence, our main conclusions are the following:

- the highest seasonal temperatures (the "warm seasons" criteria) and RSL lengthening are not well correlated for Coprates Chasma sites and Rauna crater site for dry and wet models; in general, RSL lengthening occurs for varying surface temperature ranges from one site to another (figure 16);
- RSL seasonal temperature variations are inconsistent with most of water induced triggering mechanisms, involving water/brines melting/freezing cycles for both models;
- RSL streaks are located within channels of probably few tenth centimeters depth. Our insolation computations (figures 11 and 12 suggest that small scale topography features have a non negligible effect on surface heating by the sun);
- if we consider that RSL are produced by a single mechanism, dry mechanisms may be preferred, as it does not involve water or salts, whereas dust or grains are abundant. Moreover, a close link with atmosphere is favored, as RSL activity reinforcement is observed after dust storms.

Hence, we suggest that winds and dust transport are the best explanation for RSL activity regarding the widespread spatial distribution of that flows (Stillman, 2018), well correlated with large scale wind streaks (Thomas et al., 1981). At RSL scale, we show that temperature gradients can be significant due to local grooves associated with RSL. Regional winds are modified by regional and local topographies (wind slopes, Spiga et al., 2011), insolation and temperature gradients (e.g. Gierasch and Sagan, 1971). Local and regional wind circulations and interactions with the surface may be further investigated (assessing surface friction and erosion, wind velocity) to decipher if this mechanism is suitable to trigger such flows on contemporary Mars.

Acknowledgements

The authors would like to thank D. E. Stillman and M. Vincendon for their careful reviews which significantly improve the quality of this manuscript.

RSL source mechanisms	Likelihood and observations
Melting Ice (Chevrier and Rivera-Valentin, 2012; Stillman et al., 2014)	Unlikely, we lack ice at equatorial latitudes and computed temperatures do not match with the observed seasonality. Surficial liquid water is not detected yet.
Brines (McEwen et al., 2011, 2014)	Unlikely, temperature variations are inconsistent with melting or freezing cycles, except if we have different brines at the origin of RSL. Surficial liquid water is not detected yet.
Salts deliquescence-efflorescence (Gough et al., 2011, 2014, 2016)	Unlikely, it seems odd that deliquescent salts are concentrated on low-albedo areas. Moreover, we need estimations of local RH on RSL site to know if deliquescence and efflorescence occur on right timing.
Subsurface aquifers (Abotalib and Heggy, 2019; Stillman et al., 2016, 2017)	Unlikely, there is no reliable evidence for deep aquifers at RSL locations nor connections from aquifers to the surface.
Granular flows (Dundas, 2020; Dundas et al., 2017b; Schmidt et al., 2017)	Possible for RSL sites on where we have shadowing, but we need further studies. Not suitable to explain granular flows on dunes or RSL presence on slopes with no boulders on top of them.
Winds (Dundas et al., 2017a; Dundas, 2020; Vincendon et al., 2019)	Likely, RSL are located on low-albedo areas, which indicates a close relationship with ground physical properties, and may be linked to poor dust coverage regions. RSL activity created by dust removal and deposition is consistent with the observed activity and explain the limited correlation with surface temperatures. Small scale surface topography can probably reinforce winds through high thermal gradient.
Hybrid process (Massé et al., 2016; Raack et al., 2017)	Unlikely, some RSL form when temperature are far below the melting point of water (273 K) whereas RSL-like features are formed in superheating environments for the laboratory experiments ($>$ 273 K, at 288 for Massé et al., 2016 and 297 K for Raack et al., 2017). Liquid water is not detected yet.

Table 4: Table summarizing the different mechanisms at the origin of the RSL. Main studies are cited and some observations are given in order to state on each hypothesis likelihood.

References

A. Z. Abotalib and E. Heggy. A deep groundwater origin for recurring slope lineae on mars. *Nature Geoscience*, 12(4):235, 2019. doi: 10.1038/s41561-019-0327-5.

C. H. Acton. Ancillary data services of nasa's navigation and ancillary information facility. *Planetary and Space Science*, 44(1):65–70, 1996. doi: 10.1016/0032-0633(95)00107-7.

V. Baker, R. Strom, V. Gulick, J. Kargel, G. Komatsu, and V. Kale. Ancient oceans, ice sheets and the hydrological cycle on mars. *Nature*, 352(6336):589, 1991. doi: 10.1038/352589a0.

J. L. Bandfield, V. E. Hamilton, and P. R. Christensen. A global view of martian surface compositions from mgs-tes. *Science*, 287(5458):1626–1630, 2000. doi: 10.1126/science.287.5458.1626.

P. A. Burrough, R. McDonnell, R. A. McDonnell, and C. D. Lloyd. *Principles of geographical information systems*. Oxford university press, 2015.

V. F. Chevrier and E. G. Rivera-Valentin. Formation of recurring slope lineae by liquid brines on present-day mars. *Geophysical Research Letters*, 39(21), 2012. doi: 10.1029/2012GL054119.

M. Chojnacki, A. McEwen, C. Dundas, L. Ojha, A. Urso, and S. Sutton. Geologic context of recurring slope lineae in melas and coprates chasmata, mars. *Journal of Geophysical Research: Planets*, 121 (7):1204–1231, 2016. doi: 10.1002/2015JE004991.

P. R. Christensen, J. L. Bandfield, V. E. Hamilton, S. W. Ruff, H. H. Kieffer, T. N. Titus, M. C. Malin, R. V. Morris, M. D. Lane, R. Clark, et al. Mars global surveyor thermal emission spectrometer experiment: investigation description and surface science results. *Journal of Geophysical Research: Planets*, 106(E10):23823–23871, 2001. doi: 10.1029/2000JE001370.

P. R. Christensen, B. M. Jakosky, H. H. Kieffer, M. C. Malin, H. Y. McSween, K. Nealson, G. L. Mehall, S. H. Silverman, S. Ferry, M. Caplinger, et al. The thermal emission imaging system (themis) for the mars 2001 odyssey mission. *Space Science Reviews*, 110(1-2):85–130, 2004. doi: 10.1023/B:SPAC.0000021008.16305.94.

R. Clancy, B. Sandor, M. Wolff, P. Christensen, M. Smith, J. Pearl, B. Conrath, and R. Wilson. An intercomparison of ground-based millimeter, mgs tes, and viking atmospheric temperature measurements: Seasonal and interannual variability of temperatures and dust loading in the global mars atmosphere. *Journal of Geophysical Research: Planets*, 105(E4):9553–9571, 2000. doi: 10.1029/1999JE001089.

S. Clifford and C. Bartels. The mars thermal model (marstherm): A fortran 77 finite-difference program designed for general distribution. In *Lunar and Planetary Science Conference*, volume 17, pages 142–143, 1986.

C. Cunningham, I. A. Nesnas, and W. L. Whittaker. Improving slip prediction on mars using thermal inertia measurements. *Autonomous Robots*, pages 1–19, 2017. doi: 10.1007/s10514-018-9796-4.

C. De Beule, G. Wurm, T. Kelling, M. Küpper, T. Jankowski, and J. Teiser. The martian soil as a planetary gas pump. *Nature Physics*, 10(1):17–20, 2014. doi: 10.1038/nphys2821.

C. Dundas, A. McEwen, M. Chojnacki, M. Milazzo, and S. Byrne. A granular flow model for recurring slope lineae on mars. In *Lunar and Planetary Science Conference*, volume 48, 2017a.

C. M. Dundas. An aeolian grainflow model for martian recurring slope lineae. *Icarus*, page 113681, 2020. doi: 10.1016/j.icarus.2020.113681.

C. M. Dundas, A. S. McEwen, M. Chojnacki, M. P. Milazzo, S. Byrne, J. N. McElwaine, and A. Urso. Granular flows at recurring slope lineae on mars indicate a limited role for liquid water. *Nature geoscience*, 10(12):903, 2017b. doi: 10.1038/s41561-017-0012-5.

C. S. Edwards and S. Piqueux. The water content of recurring slope lineae on mars. *Geophysical Research Letters*, 43(17):8912–8919, 2016. doi: 10.1002/2016GL070179.

W. C. Feldman, T. H. Prettyman, S. Maurice, J. J. Plaut, D. L. Bish, D. T. Vaniman, M. T. Mellon, A. E. Metzger, S. W. Squyres, S. Karunatillake, W. V. Boynton, R. C. Elphic, H. O. Funsten, D. J. Lawrence, and R. L. Tokar. Global distribution of near-surface hydrogen on mars. *Journal of Geophysical Research: Planets*, 109(E9), 2004a. doi: 10.1029/2003JE002160.

E. J. Gaidos. Cryovolcanism and the recent flow of liquid water on mars. *Icarus*, 153(1):218–223, 2001. doi: 10.1006/icar.2001.6649.

P. Gierasch and C. Sagan. A preliminary assessment of martian wind regimes. *Icarus*, 14(3):312–318, 1971. doi: 10.1016/0019-1035(71)90003-0.

R. Gough, V. Chevrier, K. Baustian, M. Wise, and M. Tolbert. Laboratory studies of perchlorate phase transitions: Support for metastable aqueous perchlorate solutions on mars. *Earth and Planetary Science Letters*, 312(3):371–377, 2011. doi: 10.1016/j.epsl.2011.10.026.

R. Gough, V. Chevrier, and M. Tolbert. Formation of aqueous solutions on mars via deliquescence of chloride–perchlorate binary mixtures. *Earth and Planetary Science Letters*, 393:73–82, 2014. doi: 10.1016/j.epsl.2014.02.002.

R. Gough, V. Chevrier, and M. Tolbert. Formation of liquid water at low temperatures via the deliquescence of calcium chloride: Implications for antarctica and mars. *Planetary and Space Science*, 131:79–87, 2016. doi: 10.1016/j.pss.2016.07.006.

R. M. Haberle, C. P. McKay, J. Schaeffer, N. A. Cabrol, E. A. Grin, A. P. Zent, and R. Quinn. On the possibility of liquid water on present-day mars. *Journal of Geophysical Research: Planets*, 106 (E10):23317–23326, 2001. doi: 10.1029/2000JE001360.

S. L. Hess, R. M. Henry, and J. E. Tillman. The seasonal variation of atmospheric pressure on mars as affected by the south polar cap. *Journal of Geophysical Research: Solid Earth*, 84(B6):2923–2927, 1979. doi: 10.1029/2000JE001360.

H. H. Kieffer, T. Martin, A. R. Peterfreund, B. M. Jakosky, E. D. Miner, and F. D. Palluconi. Thermal and albedo mapping of mars during the viking primary mission. *Journal of Geophysical Research*, 82(28):4249–4291, 1977. doi: 10.1029/JS082i028p04249.

R. Kirk, E. Howington-Kraus, M. Rosiek, J. Anderson, B. Archinal, K. Becker, D. Cook, D. Galuszka, P. Geissler, T. Hare, et al. Ultrahigh resolution topographic mapping of mars with mro hirise stereo images: Meter-scale slopes of candidate phoenix landing sites. *Journal of Geophysical Research: Planets*, 113(E3), 2008. doi: 10.1029/2007JE003000.

C. Leyrat, R. D. Lorenz, and A. Le Gall. Probing pluto's underworld: Ice temperatures from microwave radiometry decoupled from surface conditions. *Icarus*, 268:50–55, 2016. doi: 10.1016/j.icarus.2015.12.016.

J.-B. Madeleine, F. Forget, E. Millour, L. Montabone, and M. Wolff. Revisiting the radiative impact of dust on mars using the lmd global climate model. *Journal of Geophysical Research: Planets*, 116 (E11), 2011. doi: 10.1029/2011JE003855.

F. J. Martín-Torres, M.-P. Zorzano, P. Valentín-Serrano, A.-M. Harri, M. Genzer, O. Kemppinen, E. G. Rivera-Valentin, I. Jun, J. Wray, M. B. Madsen, et al. Transient liquid water and water activity at gale crater on mars. *Nature Geoscience*, 8(5):357, 2015. doi: 10.1038/ngeo2412.

M. Massé, S. J. Conway, J. Gargani, M. R. Patel, K. Pasquon, A. McEwen, S. Carpy, V. Chevrier, M. R. Balme, L. Ojha, et al. Transport processes induced by metastable boiling water under martian surface conditions. *Nature Geoscience*, 9(6):425, 2016. doi: 10.1038/ngeo2706.

A. S. McEwen, E. M. Eliason, J. W. Bergstrom, N. T. Bridges, C. J. Hansen, W. A. Delamere, J. A. Grant, V. C. Gulick, K. E. Herkenhoff, L. Keszthelyi, et al. Mars reconnaissance orbiter's high resolution imaging science experiment (hirise). *Journal of Geophysical Research: Planets*, 112(E5), 2007. doi: 10.1029/2005JE002605.

A. S. McEwen, L. Ojha, C. M. Dundas, S. S. Mattson, S. Byrne, J. J. Wray, S. C. Cull, S. L. Murchie, N. Thomas, and V. C. Gulick. Seasonal flows on warm martian slopes. *Science*, 333(6043):740–743, 2011. doi: 10.1126/science.1204816.

A. S. McEwen, C. M. Dundas, S. S. Mattson, A. D. Toigo, L. Ojha, J. J. Wray, M. Chojnacki, S. Byrne, S. L. Murchie, and N. Thomas. Recurring slope lineae in equatorial regions of mars. *Nature geoscience*, 7(1):53–58, 2014. doi: 10.1038/ngeo2014.

A. S. McEwen, E. Schaefer, S. Sutton, and M. Chojnacki. Remarkably Widespread RSL Activity Following the Great Martian Dust Storm of 2018. In *EPSC-DPS Joint Meeting 2019*, volume 2019, pages EPSC–DPS2019–557, Sept. 2019.

T. Michaels and S. Rafkin. Meteorological predictions for candidate 2007 phoenix mars lander sites using the mars regional atmospheric modeling system (mrams). *Journal of Geophysical Research: Planets*, 113(E3), 2008. doi: 10.1029/2007JE003013.

C. Millot, C. Quantin-Nataf, C. Leyrat, and M. Volat. High Resolution Digital Elevation Model Errors Propagation on Computed Slopes. In *Lunar and Planetary Science Conference*, Lunar and Planetary Science Conference, page 1475, Mar. 2020.

G. Munaretto, M. Pajola, G. Cremonese, C. Re, A. Lucchetti, E. Simioni, A. McEwen, A. Pommerol, P. Becerra, S. Conway, N. Thomas, and M. Massironi. Implications for the origin and evolution of martian recurring slope lineae at hale crater from cassis observations. *Planetary and Space Science*, 187:104947, 2020. ISSN 0032-0633. doi: 10.1016/j.pss.2020.104947.

S. Murchie, R. Arvidson, P. Bedini, K. Beisser, J.-P. Bibring, J. Bishop, J. Boldt, P. Cavender, T. Choo, R. Clancy, et al. Compact reconnaissance imaging spectrometer for mars (crism) on mars reconnaissance orbiter (mro). *Journal of Geophysical Research: Planets*, 112(E5), 2007. doi: 10.1029/2006JE002682.

G. Neukum and R. Jaumann. Hrsc: The high resolution stereo camera of mars express. In *Mars Express: The Scientific Payload*, volume 1240, pages 17–35, 2004.

F. Nimmo and K. Tanaka. Early crustal evolution of mars. *Annu. Rev. Earth Planet. Sci.*, 33:133–161, 2005. doi: 10.1146/annurev.earth.33.092203.122637.

L. Ojha, J. J. Wray, S. L. Murchie, A. S. McEwen, M. J. Wolff, and S. Karunatillake. Spectral constraints on the formation mechanism of recurring slope lineae. *Geophysical Research Letters*, 40 (21):5621–5626, 2013. doi: 10.1002/2013GL057893.

L. Ojha, A. McEwen, C. Dundas, S. Byrne, S. Mattson, J. Wray, M. Masse, and E. Schaefer. Hirise observations of recurring slope lineae (rsl) during southern summer on mars. *Icarus*, 231:365–376, 2014. doi: 10.1016/j.icarus.2013.12.021.

L. Ojha, M. B. Wilhelm, S. L. Murchie, A. S. McEwen, J. J. Wray, J. Hanley, M. Massé, and M. Chojnacki. Spectral evidence for hydrated salts in recurring slope lineae on mars. *Nature Geoscience*, 8 (11):829–832, 2015. doi: 10.1038/ngeo2546.

S. Piqueux and P. R. Christensen. A model of thermal conductivity for planetary soils: 2. theory for cemented soils. *Journal of Geophysical Research: Planets*, 114(E9), 2009. doi: 10.1029/2008JE003309.

S. Piqueux and P. R. Christensen. Temperature-dependent thermal inertia of homogeneous martian regolith. *Journal of Geophysical Research: Planets*, 116(E7), 2011. doi: 10.1029/2011JE003805.

J. B. Pollack and C. Sagan. Secular changes and dark-area regeneration on mars. *Icarus*, 6(1-3): 434–439, 1967. doi: 10.1016/0019-1035(67)90036-X.

J. B. Pollack, J. F. Kasting, S. M. Richardson, and K. Poliakoff. The case for a wet, warm climate on early mars. *Icarus*, 71(2):203–224, 1987. doi: 10.1016/0019-1035(87)90147-3.

N. E. Putzig. *Thermal inertia and surface heterogeneity on Mars*. 2006.

J. Raack, S. J. Conway, C. Herny, M. R. Balme, S. Carpy, and M. R. Patel. Water induced sediment levitation enhances downslope transport on mars. *Nature communications*, 8(1):1151, 2017. doi: 10.1038/s41467-017-01213-z.

D. Rea. The darkening wave on mars. *Nature*, 201(4923):1014, 1964. doi: 10.1038/2011014a0.

H. Savijärvi and T. Siili. The martian slope winds and the nocturnal pbl jet. *Journal of the Atmospheric Sciences*, 50(1):77–88, 1993. doi: 10.1175/1520-0469.

F. Schmidt, F. Andrieu, F. Costard, M. Kocifaj, and A. G. Meresescu. Formation of recurring slope lineae on mars by rarefied gas-triggered granular flows. *Nature Geoscience*, 10(4):270–273, 2017. doi: 10.1038/ngeo2917.

N. Schorghofer, J. Levy, and T. Goudge. High-resolution thermal environment of recurring slope lineae in palikir crater, mars, and its implications for volatiles. *Journal of Geophysical Research: Planets*, 2019. doi: 10.1029/2019JE006083.

A. Spiga and F. Forget. Fast and accurate estimation of solar irradiance on martian slopes. *Geophysical Research Letters*, 35(15), 2008. doi: 10.1029/2008GL034956.

A. Spiga, F. Forget, J.-B. Madeleine, L. Montabone, S. R. Lewis, and E. Millour. The impact of martian mesoscale winds on surface temperature and on the determination of thermal inertia. *Icarus*, 212 (2):504–519, 2011. doi: 10.1016/j.icarus.2011.02.001.

D. E. Stillman. Unraveling the mysteries of recurring slope lineae. In *Dynamic Mars*, pages 51–85. Elsevier, 2018. doi: 10.1016/B978-0-12-813018-6.00002-9.

D. E. Stillman and R. E. Grimm. Two pulses of seasonal activity in martian southern mid-latitude recurring slope lineae (rsl). *Icarus*, 302:126–133, 2018. doi: 10.1016/j.icarus.2017.10.026.

D. E. Stillman, T. I. Michaels, R. E. Grimm, and K. P. Harrison. New observations of martian southern mid-latitude recurring slope lineae (rsl) imply formation by freshwater subsurface flows. *Icarus*, 233: 328–341, 2014. doi: 10.1016/j.icarus.2014.01.017.

D. E. Stillman, T. I. Michaels, R. E. Grimm, and J. Hanley. Observations and modeling of northern mid-latitude recurring slope lineae (rsl) suggest recharge by a present-day martian briny aquifer. *Icarus*, 265:125–138, 2016. doi: 10.1016/j.icarus.2015.10.007.

D. E. Stillman, T. I. Michaels, and R. E. Grimm. Characteristics of the numerous and widespread recurring slope lineae (rsl) in valles marineris, mars. *Icarus*, 285:195–210, 2017. doi: 10.1016/j.icarus.2016.10.025.

D. E. Stillman, B. D. Bue, K. L. Wagstaff, K. M. Primm, T. I. Michaels, and R. E. Grimm. Evaluation of wet and dry recurring slope lineae (rsl) formation mechanisms based on quantitative mapping of rsl in garni crater, valles marineris, mars. *Icarus*, 335:113420, 2020. doi: 10.1016/j.icarus.2019.113420.

J. L. Sutton, C. B. Leovy, and J. E. Tillman. Diurnal variations of the martian surface layer meteorological parameters during the first 45 sols at two viking lander sites. *Journal of the atmospheric sciences*, 35(12):2346–2355, 1978. doi: 10.1175/1520-0469.

S. Sutton, M. Chojnacki, A. Kilgallon, and H. Team. Precision and accuracy of simultaneously collected hirise digital terrain models. In *46th Lunar and Planetary Science Conference*, page Abstract #3010, Houston, 2015. Lunar and Planetary Institute.

M. A. Szwast, M. I. Richardson, and A. R. Vasavada. Surface dust redistribution on mars as observed by the mars global surveyor and viking orbiters. *Journal of Geophysical Research: Planets*, 111 (E11), 2006. doi: 10.1029/2005JE002485.

M. Tebolt, J. Levy, T. Goudge, and N. Schorghofer. Slope, elevation, and thermal inertia trends of martian recurring slope lineae initiation and termination points: Multiple possible processes occurring on coarse, sandy slopes. *Icarus*, 338:113536, 2020. ISSN 0019-1035. doi: 10.1016/j.icarus.2019.113536.

N. Thomas, G. Cremonese, R. Ziethe, M. Gerber, M. Brändli, G. Bruno, M. Erismann, L. Gambicorti, T. Gerber, K. Ghose, et al. The colour and stereo surface imaging system (cassis) for the exomars trace gas orbiter. *Space science reviews*, 212(3-4):1897–1944, 2017. doi: 10.1007/s11214-017-0421-1.

P. Thomas, J. Veverka, S. Lee, and A. Bloom. Classification of wind streaks on mars. *Icarus*, 45(1): 124–153, 1981. doi: 10.1016/0019-1035(81)90010-5.

M. Vincendon, C. Pilorget, J. Carter, and A. Stcherbinine. Observational evidence for a dry dust-wind origin of mars seasonal dark flows. *Icarus*, 2019. doi: 10.1016/j.icarus.2019.02.024.

J. T. Wilson, V. R. Eke, R. J. Massey, R. C. Elphic, W. C. Feldman, S. Maurice, and L. F. Teodoro. Equatorial locations of water on mars: Improved resolution maps based on mars odyssey neutron spectrometer data. *Icarus*, 2018. doi: 10.1016/j.icarus.2017.07.028.

M. T. Zuber. The crust and mantle of mars. *Nature*, 412(6843):220, 2001. doi: 10.1038/35084163.

M. T. Zuber, D. Smith, S. Solomon, D. Muhleman, J. Head, J. Garvin, J. Abshire, and J. Bufton. The mars observer laser altimeter investigation. *Journal of Geophysical Research: Planets*, 97(E5): 7781–7797, 1992. doi: 10.1029/92JE00341.